

Master Thesis

**Exploring the existence of prebiotic species:
ALMA observations of amine-containing
organic molecule in star-forming regions.**

Harumi Minamoto

17M01629

Nomura Laboratory

Department of Earth and Planetary Sciences, Tokyo Institute of Technology

January 23, 2019

Abstract

A variety of complex organic molecules have been observed for decades in the interstellar medium. Some of them are considered to be delivered to the primordial Earth by comets, and contributed to the chemical evolution leading to terrestrial life. One example of such prebiotic species is amino acid. Glycine, the simplest amino acid, has been detected in comet 67P/C-G but its presence in molecular clouds is still uncertain.

In this work we analyze the ALMA archival data toward 3 star-forming regions, Orion Kleinmann-Low nebula (hereafter Orion-KL), IRAS 16293-2422 (IRAS 16293), and L483, to search methylamine (CH_3NH_2), which is suggested as precursors to glycine.

As a result of analysis, we found 8 candidate emission at the hot core region in Orion-KL. By using the rotation diagram method, we evaluated its tentative column density and rotational temperature to be $(5.5^{+1.6}_{-1.1}) \times 10^{14} \text{ cm}^{-2}$ and $95.4^{+15.5}_{-11.7} \text{ K}$, respectively. On the other hand, CH_3NH_2 is not detected and stringent upper limit column densities are determined in IRAS 16293 and L483.

Contents

Abstract	i
1 Introduction	1
1.1 Glycine and methylamine	1
1.2 Star forming region	2
1.2.1 Orion Kleinmann-Low nebula	2
1.2.2 IRAS 16293-2422	2
1.2.3 L483	2
1.3 Radio observation	3
1.3.1 Atacama Large Millimeter Array	4
1.4 Purpose of this work	4
2 Methylamine survey in Orion-KL	5
2.1 Observation data	5
2.2 Analysis	6
2.2.1 Reduction of SV data	6
2.2.2 Line identification	10
2.3 Results	11
2.3.1 Overall CH_3NH_2 distribution	11
2.3.2 Spectrum	20
2.4 Discussion	22
2.4.1 Column density and Rotation temperature	22

2.4.2	Undetectable lines	23
3	Methylamine survey in low mass star-forming regions	29
3.1	Review of low mass star-forming region	30
3.2	Analysis	30
3.3	IRAS 16293	30
3.3.1	Observation data	30
3.3.2	Results	30
3.4	L483	32
3.4.1	Observation data	32
3.4.2	Results	32
4	Discussion	34
5	Conclusions	35
A	Distribution of methylamine lines contaminated by other molecular line emission in Orion-KL	36
A.1	Integrated intensity maps	36
A.2	Channel maps	40
Acknowledgments		56
References		57

Chapter 1

Introduction

1.1 Glycine and methylamine

Methylamine (CH_3NH_2) is considered as a precursor of the simplest amino acid glycine. Recent experimental studies have shown several reaction pathways to forming glycine in water containing ices starting from CH_3NH_2 and CO_2 subjected to high energy electrons (Holtom et al., 2005) or UV radiation (Bossa et al., 2009; Lee et al., 2009). Under similar conditions glycine can decompose to yield methylamine and CO_2 (Ehrenfreund et al., 2001). Interstellar CH_3NH_2 was first detected toward Sgr B2 at 3.5 cm (Fourikis et al., 1974) and at 3mm (Kaifu et al., 1974). Recently, CH_3NH_2 has been detected in cometary samples of the Stardust mission (Glavin et al., 2008) and comet 67P/C-G (Altwegg et al., 2016, 2017).

1.2 Star forming region

1.2.1 Orion Kleinmann-Low nebula

This Orion Kleinmann-Low nebula (hereafter Orion-KL) to be studied is an infrared nebula in the Orion nebula, which is located approximately 388 ± 5 pc away from the sun (Kounkel et al., 2017). In this region, it is a very active area where a huge star with 30 times the mass of the sun is born, and a lot of molecules are observed also in line survey observing a wide range of frequencies. This Orion-KL is a large mass star formation region closest to the sun and has strong radiant intensity and still many molecules exist. Since this region was discovered in 1967, many studies including line survey have been done so far. In Orion-KL, a place called Hot core and Compact ridge is known as a region where many organic molecules exist. Hot core is known as a high-density (10^6 cm^{-3}) area with a warm ($\sim 150 \text{ K}$), compact ($< 0.05 \text{ pc}$), and Compact ridge is also known to be a warm and dense region. However, the chemical properties are different, while many molecules containing nitrogen (for example, NH_3 , CH_3CN , etc.) are observed in Hot core, while molecules containing oxygen (eg, CH_3OH , CH_3OCH_3 , etc.) are observed in Compact ridge.

1.2.2 IRAS 16293-2422

1.2.3 L483

1.3 Radio observation

The observation of outer space by radio waves has been established as one of observation methods of outer space since the discovery of the first cosmic radio wave in the 1930s by Karl G. Jansky and the creation of the world's first radio telescope by Grote Reber. It has made great progress with the progress of radar technology during World War II. Since then, observations have been carried out even at wavelengths such as X-rays and infrared, unraveling the wonders of the universe that can not be known with only visible light. However, due to the influence of atmospheric absorption, visible light, radio waves and part of infrared rays are observable from the ground of all wavelengths. In the area of radio waves, frequencies below 20 MHz do not pass through the ionosphere, and at high frequencies they are easily absorbed by atmospheric oxygen and water vapor. For this reason, it is appropriate to install the radio telescope in places with high altitude and low water vapor. Different phenomena can be captured in outer space by the wavelengths observed, such as visible light and infrared light, but in observation of outer space by radio waves there is a feature not found in other wavelengths.

- We can observe low temperature objects that can not be seen with visible light.

After being born, the star radiates visible light, but low temperature objects before the star is born release not visible light but radio waves. Therefore, observations by radio waves is necessary.

- Long wavelength

Because of this feature, it is hard to be absorbed by interstellar microparticles, and it is possible to observe up to the far side.

- Easy electrical interference technology In a telescope called an interferometer, it is possible to obtain a high resolution by observing by placing a plurality of antennas apart and interfering radio waves. With this method in the radio wave range, higher resolution than observation with other wavelengths is obtained.

With the above characteristics, radio observation occupies an important position in astronomy.

1.3.1 Atacama Large Millimeter Array

1.4 Purpose of this work

Chapter 2

Methylamine survey in Orion-KL

In this chapter, we report the tentatively detection CH_3NH_2 in Orion-KL.

2.1 Observation data

We analyzed 2 ALMA archival data. First we used Cycle 2 data (ADS/JAO.ALMA#2013.1.00553.S, Pagani et al. (2017)) We also employed the ALMA Science Verification (SV) data (ADS/JAO.ALMA#2011.0.00009.SV) at band 6 to fill up the missing frequency coverage of Cycle 2 data. Details of each data are summarized in Table 2.1.

Cycle 2 data cube was already calibrated by observers and the reduced data are available on the Internet¹. Since the SV data contained not only line emission but continuum emission, we subtracted continuum emission statistically by the method described in Section 2.2.1.

In addition, we used Common Astronomy Software Applications (CASA) software (McMullin et al., 2007) during the procedure to analyze observational data.

¹<http://cdsarc.u-strasbg.fr/viz-bin/qcat?J/A+A/604/A32>

Table 2.1: Summary of Observations

Date	Window (spw)	Frequency range (GHz)	FWHM (arcsec)	PA (degree)
29–30 December 2014	1	215.145–216.087	1.8×1.1	86
	2	216.342–217.279	1.8×1.1	84
	3	217.273–218.211	2.2×1.0	102
	4	218.204–219.141	2.2×1.0	102
	5	219.127–220.064	1.9×1.0	95
	6	219.784–220.721	1.8×1.0	95
	7	229.757–230.694	1.4×0.8	80
	8	230.699–231.636	2.1×0.9	102
	9	232.238–233.175	1.6×1.0	80
	10	233.470–234.422	1.6×0.8	90
	11	235.084–236.021	1.7×0.9	95
	12	236.267–237.206	1.6×0.9	87
	13	244.834–245.771	1.6×0.9	79
	14	245.773–246.710	1.6×0.9	79
	15	250.154–251.091	1.5×0.9	88
	16	251.079–252.016	1.3×0.8	86
20 January 2012	0–16	213.715–246.627	1.8×1.3	-1

2.2 Analysis

2.2.1 Reduction of SV data

With the advent of highly sensitive facilities such as ALMA, the spectral lines which were hindered by the noise level with previous telescope can now be detected. Most of these line-rich sources including hot cores are associated with detectable continuum emission. In the analysis of molecular emission lines, the determination and the subtraction of this continuum emission is an essential, but difficult task. Therefore, we improved the method devised in Sanchez-Monge et al. (2017) and deduced continuum subtraction in the observed UV domain (the raw visibilities measured by the interferometer). We introduce the manner and results in this section.

Determination of the continuum level

The determination of the continuum emission level of astronomical sources observed in a spectral line observing mode is based on the identification of channels free of line emission, i.e. line-free channels.

First, we obtain the spectra for which we want to estimate the continuum level. In the case of Orion-KL, many molecular emission exist in Hot core ($\text{RA}_{J2000} : 05^{\text{h}}35^{\text{m}}14^{\text{s}}.580$, $\text{Dec}_{J2000} : -05^{\circ}22'31''.029$) or Compact ridge($\text{RA}_{J2000} : 05^{\text{h}}35^{\text{m}}14^{\text{s}}.2775$, $\text{Dec}_{J2000} : -05^{\circ}22'30''.776$), so we extracted spectra from circular regions with a diameter of $1''$.0 with the coordinates indicated by Hirota et al. (2015) as the center. The peak of the distribution of the intensity values is determined with a Gaussian fit when assuming the Gaussian random error resulting in an estimate of the mean value E and the standard deviation σ . The width is small in case of pixels with little or no line emission, but for line contaminated regions the distribution becomes broader and the exact location of the peak more uncertain. Therefore, we set the range of the Gaussian fitting from 0 to $1/3$ of the peak intensity in line contaminated side, and calculated the mean value E and the standard deviation σ .

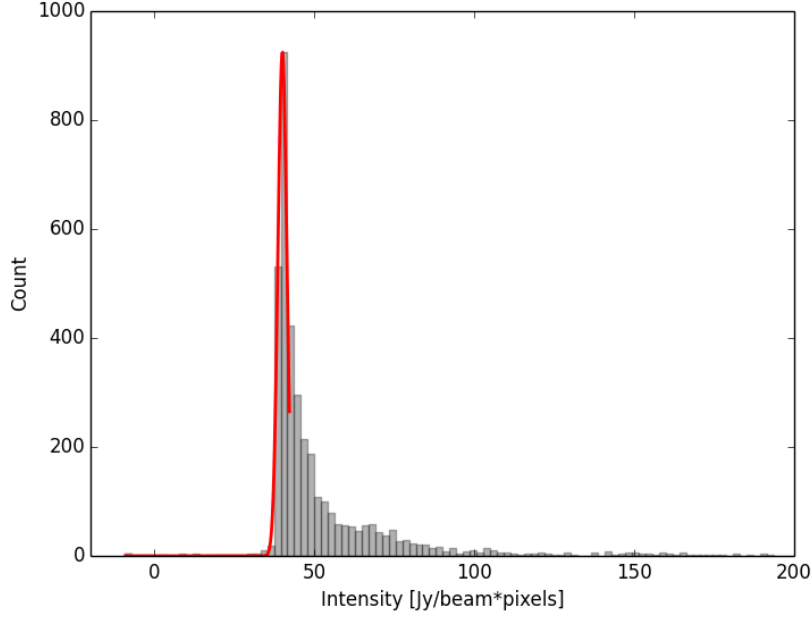


Figure 2.1: Schematic description of the process of determination of the continuum level toward Orion-KL: shown are the flux distributions of Hot core (histogram) with the resulting fit overlaid (red line).

Imaging line cubes

Subsequently, the part of the distribution within $E - 3\sigma$ is defined as line-free channels. Hot core and Compact ridges have different spectrums because of the disparate chemical composition, so we determined the line-free channels individually and subtracted the continuum in the UV domain by CASA task UVCONTSUB with channels common to the two regions. After the continuum subtraction, line cubes of Orion-KL were made using the CASA task CLEAN.

Figure 2.2 shows examples of difference spectrum towards Hot core. It can be confirmed that the continuum subtraction has succeeded.

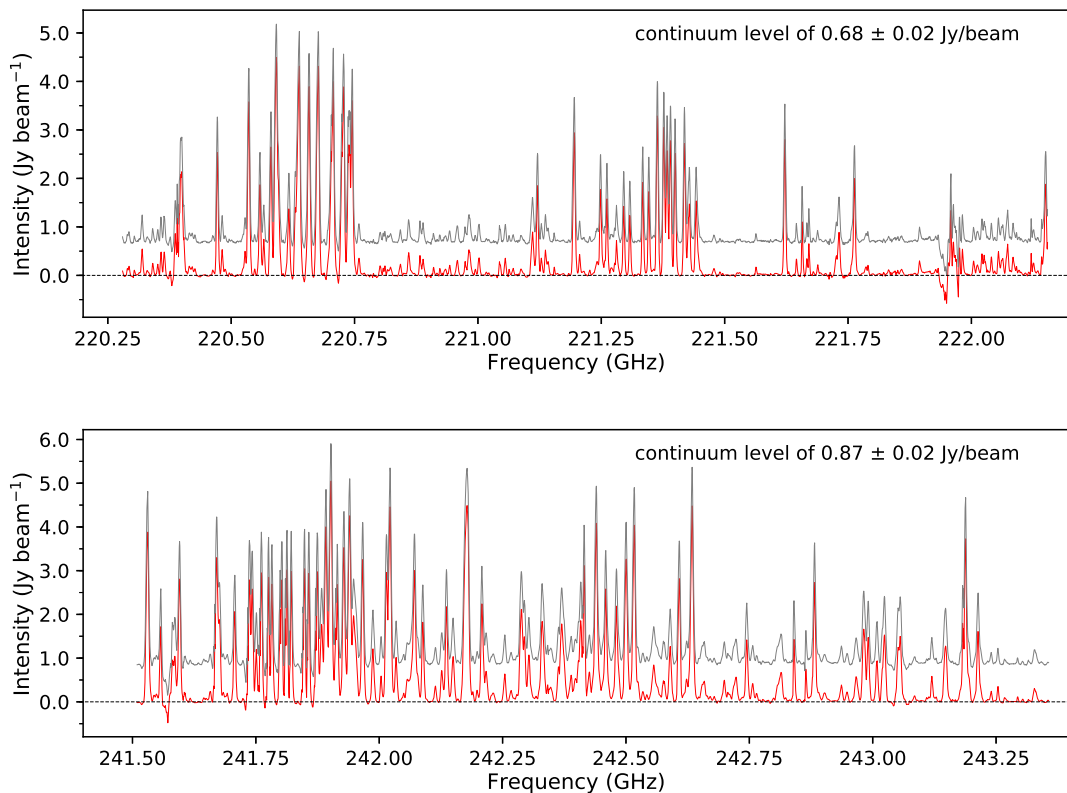


Figure 2.2: The original spectra (gray) and continuum-subtracted spectra (red) towards Hot core. The dotted line represents the base line (0 level). The continuum emission level subtracted to the original spectra, together with its uncertainty, is listed in the upper right part of each panel.

2.2.2 Line identification

In order to find out where common signals exist, we drew integrated intensity maps using CASA task IMMOMENT. The integrated velocity range is $3.0\text{-}12.0 \text{ km s}^{-1}$, corresponding to typical velocity component of Hot core ($4.8\text{-}6 \text{ km s}^{-1}$) and that of Compact ridge ($7.2\text{-}9.6 \text{ km s}^{-1}$) (Feng et al., 2015). Spectroscopic data of CH_3NH_2 are provided by Motiyenko et al. (2014) and JPL Molecular Spectroscopy catalog².

Then, since emission at the center of Hot core were found in most of integrated intensity maps, we extracted spectrum for transitions with no line blending around $\pm 2 \text{ km s}^{-1}$ from Hot core. Possible line blending ($E_u < 500 \text{ K}$) with CH_3NH_2 was investigated by JPL database, the Cologne database for molecular spectroscopy (CDMS)³, and Splatalogue⁴.

Subsequently, we estimated the systemic velocity and the line width of 217.758 GHz line, reported by Pagani et al. (2017), which does not seem contaminated by other molecular lines. At last, using these value, we obtained the integrated intensity of 6 transitions described in Table 2.2 by the Gaussian fitting.

²<http://spec.jpl.nasa.gov>

³<http://www.astro.uni-koeln.de/cdms/>

⁴<http://www.splatalogue.net/>

2.3 Results

The data obtained for CH₃NH₂ are summarized in Table 2.2. Here the rest frequencies, $S\mu^2$, the upper state energy (E_u), the quantum numbers, the peak brightness temperature, the systemic velocity (V_{LSR}) , and noise level are given. Out of 32 predicted transitions ($S\mu^2 > 25 \text{ D}^2$ and $E_u < 200 \text{ K}$) in our observational frequency range, 6 were probably identified in this data set, and are reported in Table 2.2. The remaining 18 CH₃NH₂ transitions are blended with or masked by other spectral features, or its signal are below the noise level (See Appendix A).

Table 2.2: Observed rotational transitions of CH₃NH₂ in Orion-KL

Frequency [GHz]	$S\mu^2$ [D ²]	E_u [K]	Transition (J, K_a, Γ)	peak T_B [K]	V_{LSR} [km s ⁻¹]	Noise [K]	Comments
217.758	129.88	182.05	12, 2, $B_2 \rightarrow 12, 1, B_1$	0.86(0.03)	4.73(0.08)	0.034	Reported in Pagani+17
245.202	37.84	168.31	12, 1, $B_2 \rightarrow 11, 2, B_1$	0.37(0.01)	4.51(0.08)	0.037	Reported in Pagani+17
229.908	27.37	92.71	8, 2, $A_2 \rightarrow 8, 1, A_1$	0.65(0.01)	4.91(0.03)	0.064	
235.735	82.06	92.76	8, 2, $B_2 \rightarrow 8, 1, B_1$	1.70(0.02)	4.86(0.03)	0.081	Reported in Pagani+17
242.262	60.23	60.86	6, 2, $B_2 \rightarrow 6, 1, B_1$	2.03(0.03)	4.80(0.09)	0.166	SV data
244.887	49.54	48.09	5, 2, $B_1 \rightarrow 5, 1, B_2$	1.29(0.57)	5.23(0.90)	0.043	Reported in Pagani+17

2.3.1 Overall CH₃NH₂ distribution

CH₃NH₂ emission appears mainly at Hot core and partially at IRc7. According to previous work (see e.g., Feng et al., 2015; Gong et al., 2015), N-bearing species tend to have similar peak at or near Hot core. CH₃NH₂ also shows the same trend.

In the integrated intensity map of 229.908 GHz line, emission come from the south part of Hot core. Since it can be confirmed that the velocity component is different in the channel map (see Figure 2.9), this is considered to be the emission of another molecular line.

In addition, the extended emission in Hot core and the compact structure at Compact ridge are seen in the integrated intensity map of 242.262 GHz line. These are also

considered to be emission from other molecule line by the channel map (Figure 2.8) and spectrum (Figure 2.3.2).

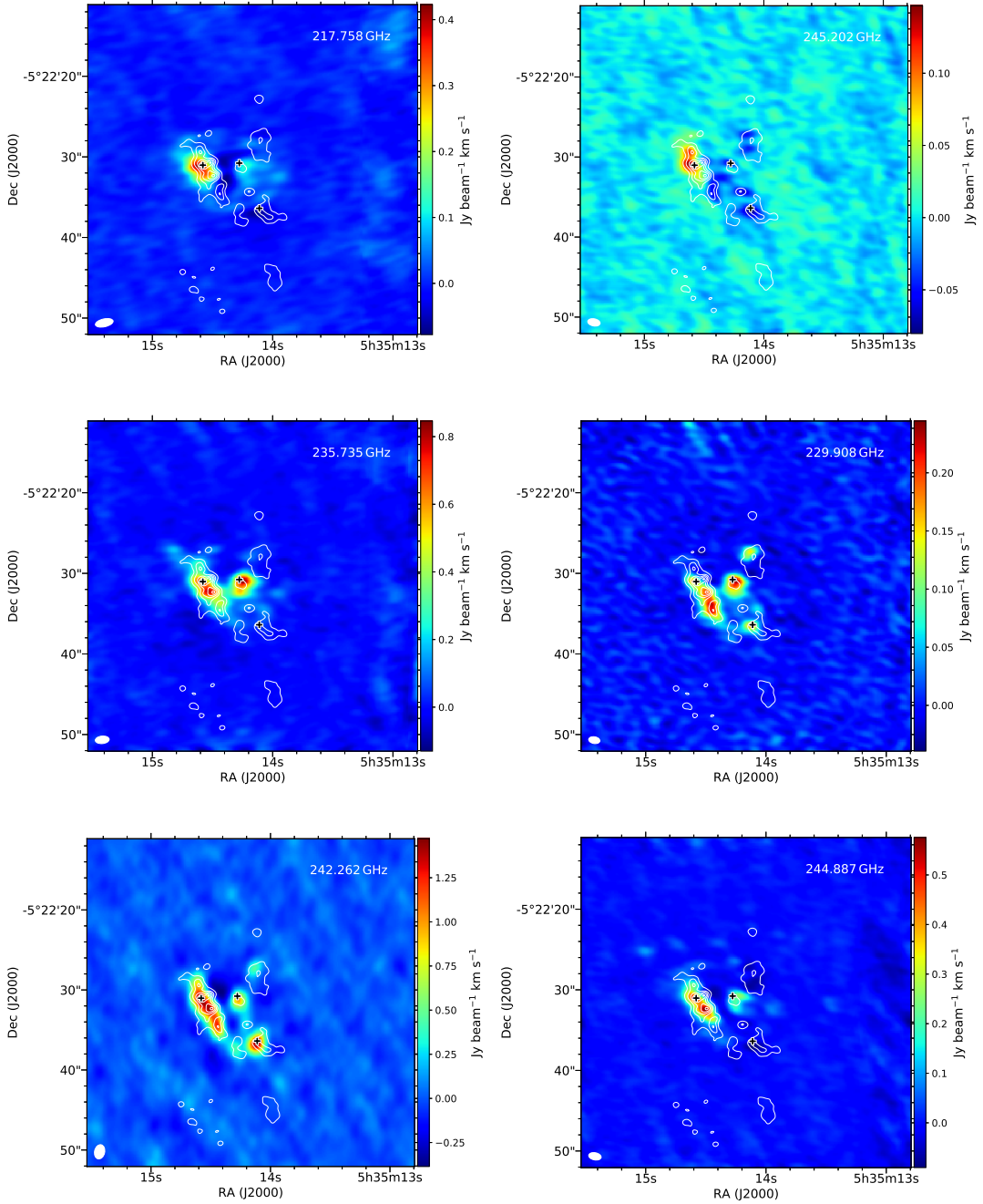


Figure 2.3: Integrated intensity maps of unblended CH_3NH_2 lines. The white contours show the 1.3 mm continuum map from Hirota et al. (2015), where the contour levels are 10 %, 30 %, 50 %, 70 %, 90 % of the peak intensity. Black crosses denote Hot core, IRc7, and Compact ridge. The rest frequency of each transition shows in the upper right part of each panel.

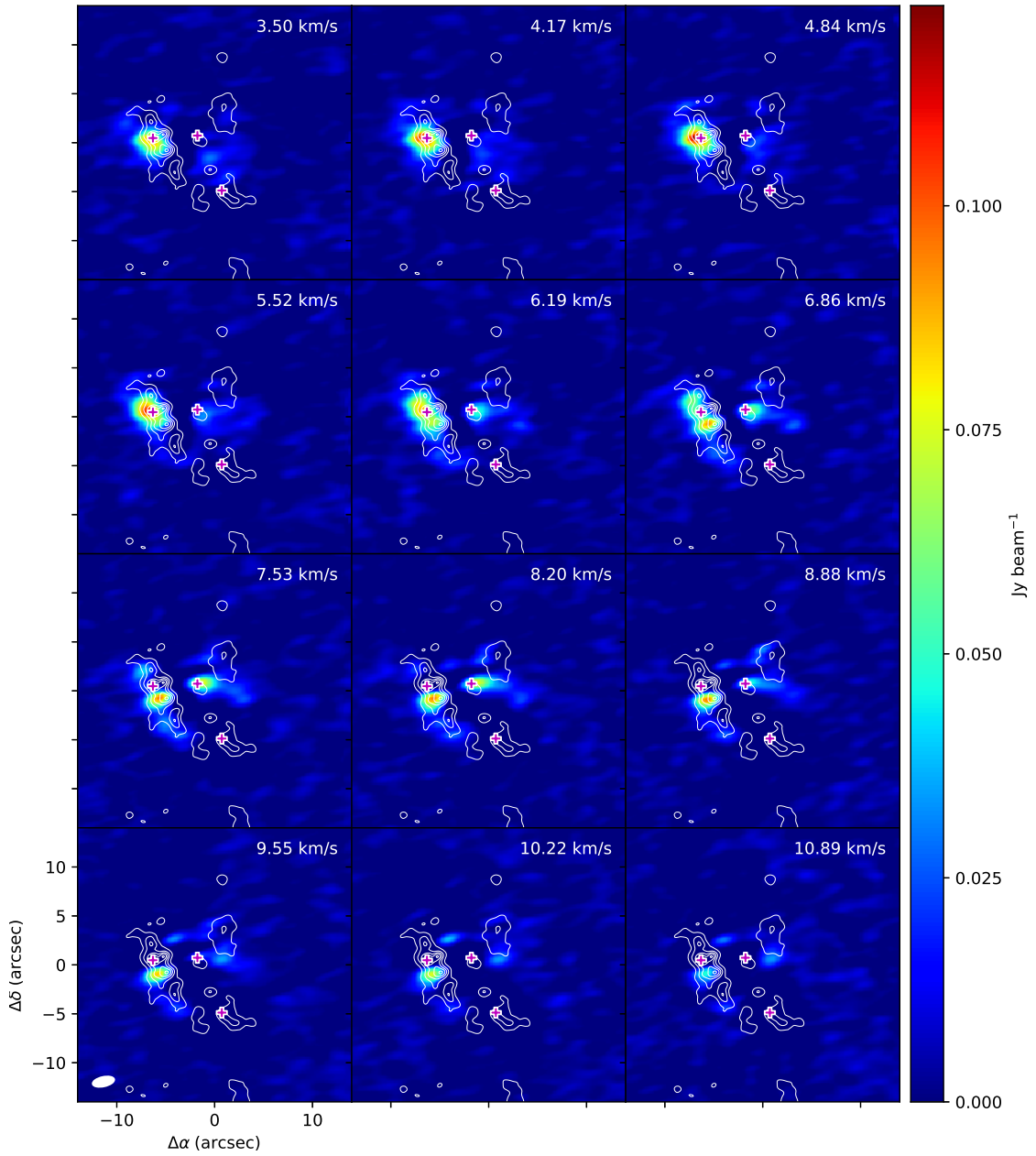


Figure 2.4: Channel map of expected unblended 217.758 GHz line show multiple velocity-dependent emission peaks: $4\text{-}6 \text{ km s}^{-1}$ towards Hot core, $7\text{-}9 \text{ km s}^{-1}$ towards IRc7. Magenta crosses denote Hot core, IRc7, and Compact ridge.

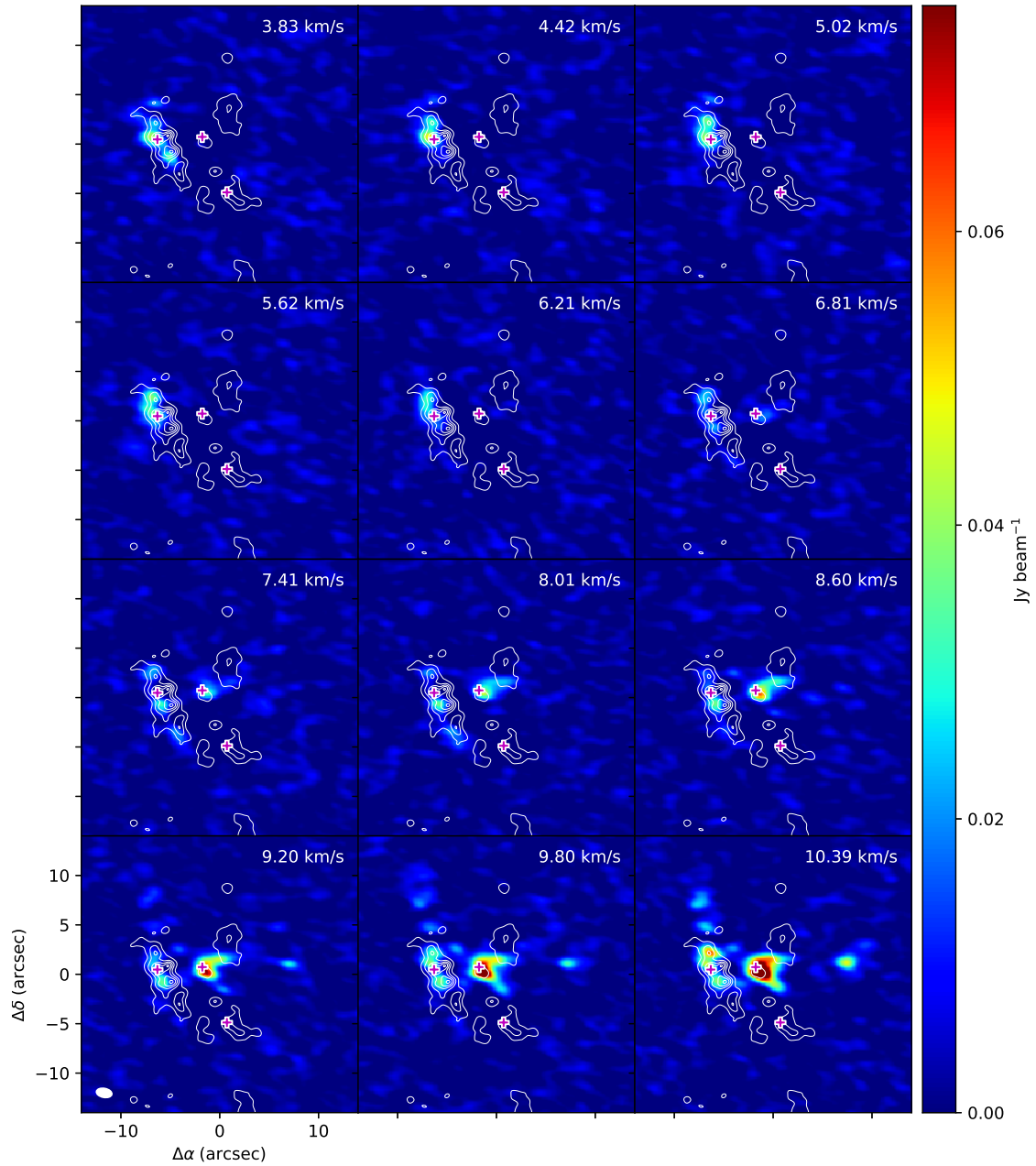


Figure 2.5: Channel map of expected unblended 245.202 GHz line.

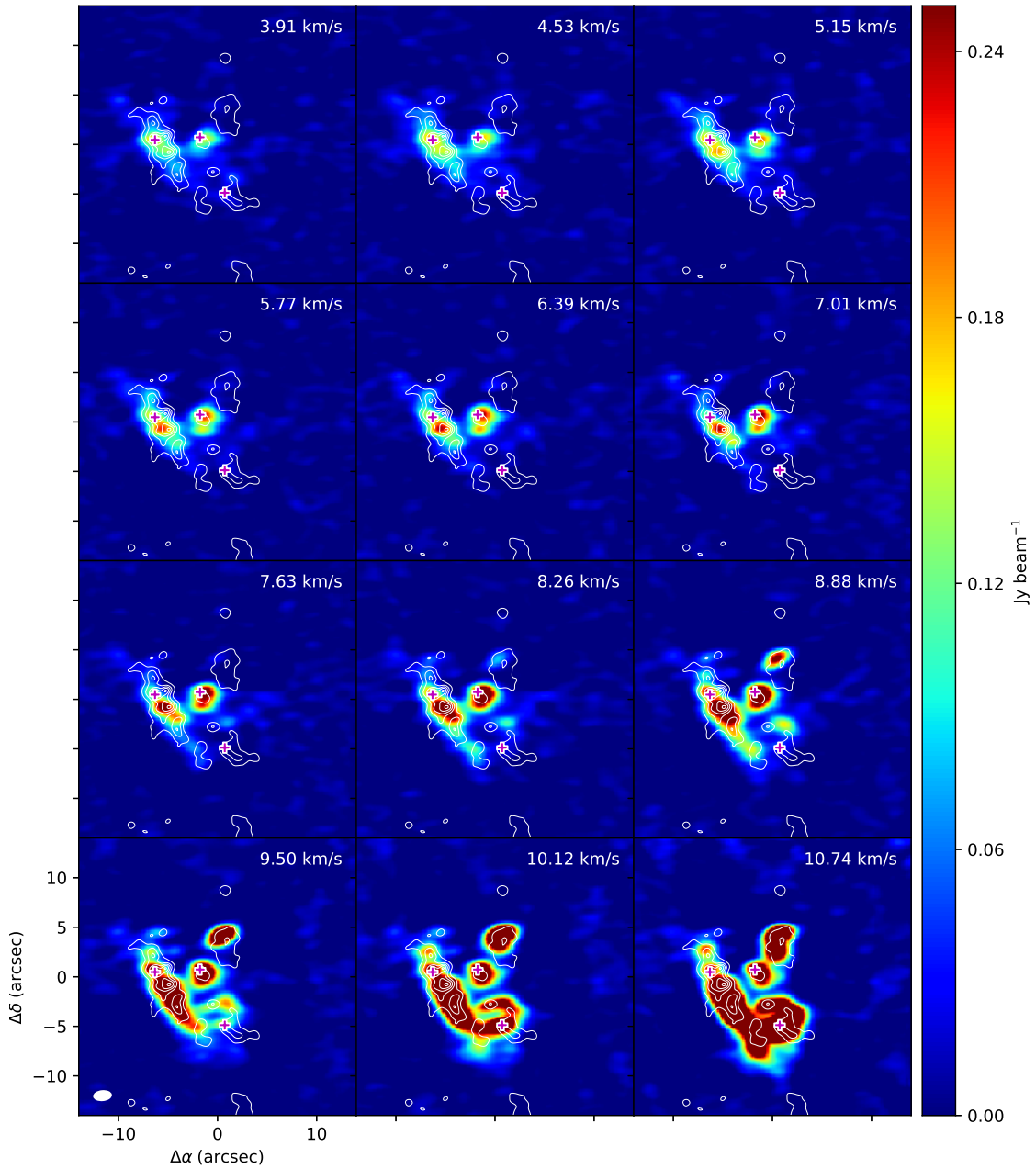


Figure 2.6: Channel map of expected unblended 235.735 GHz line.

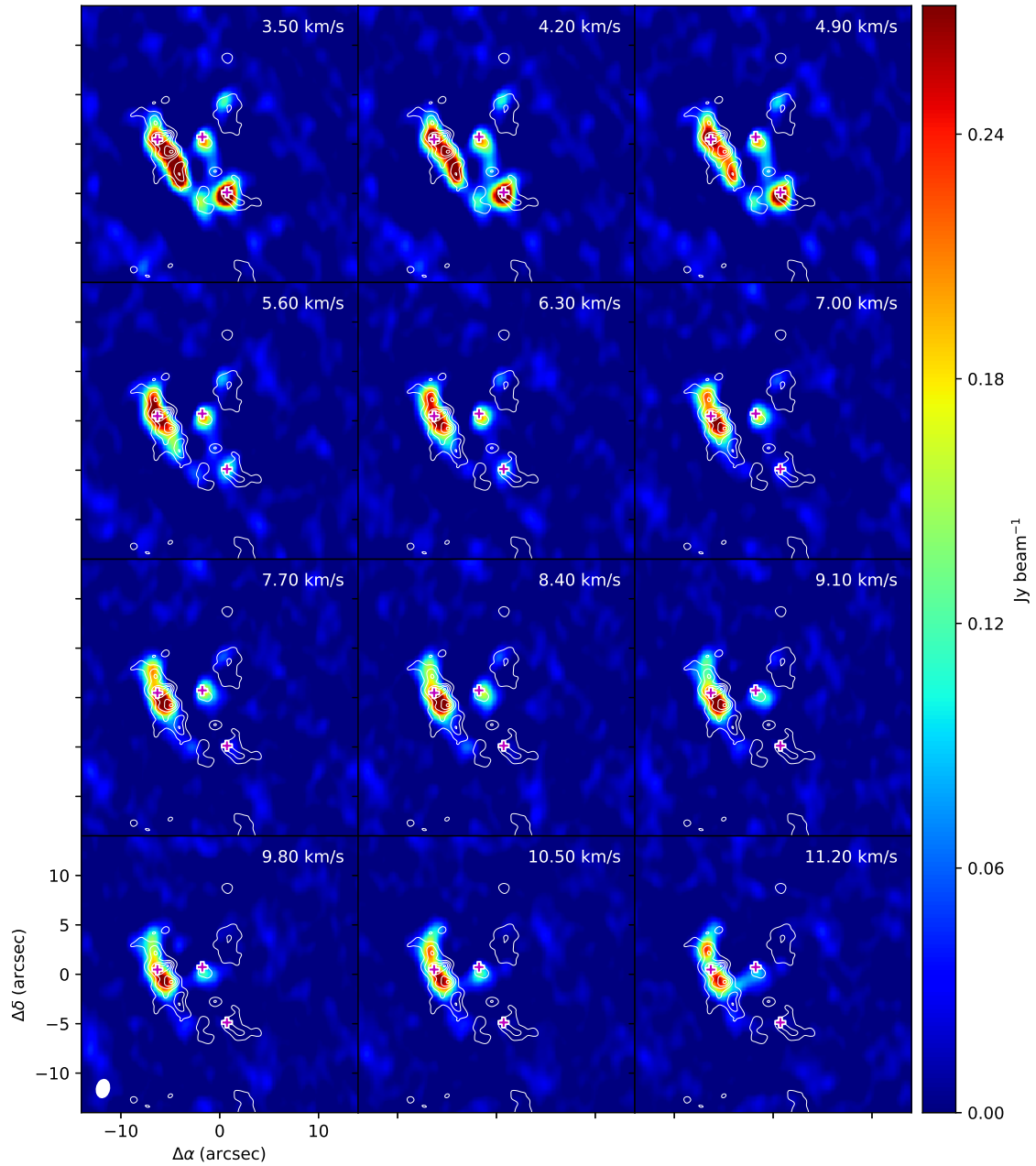


Figure 2.7: Channel map of expected unblended 242.262 GHz line.

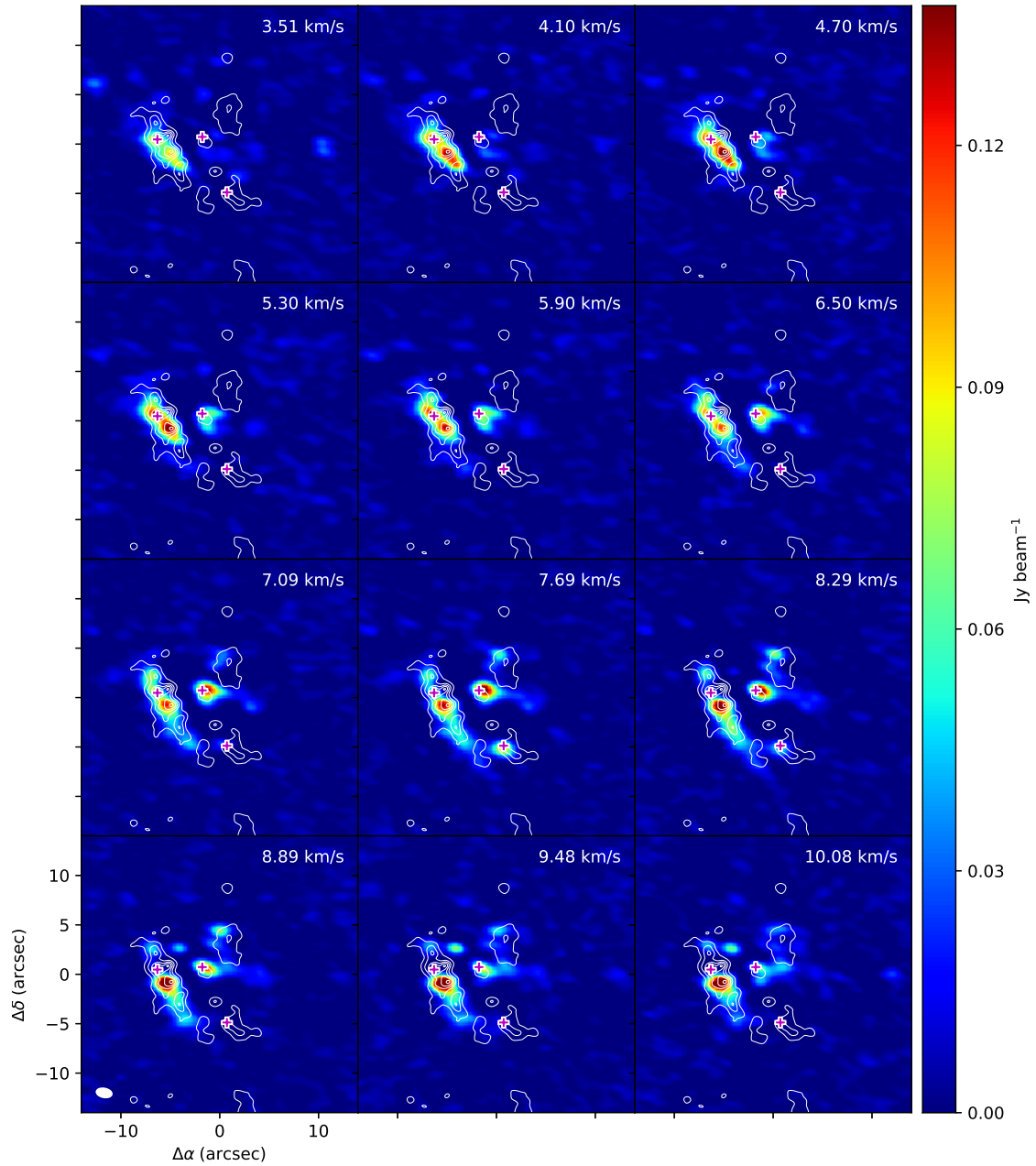


Figure 2.8: Channel map of expected unblended 244.887 GHz line.

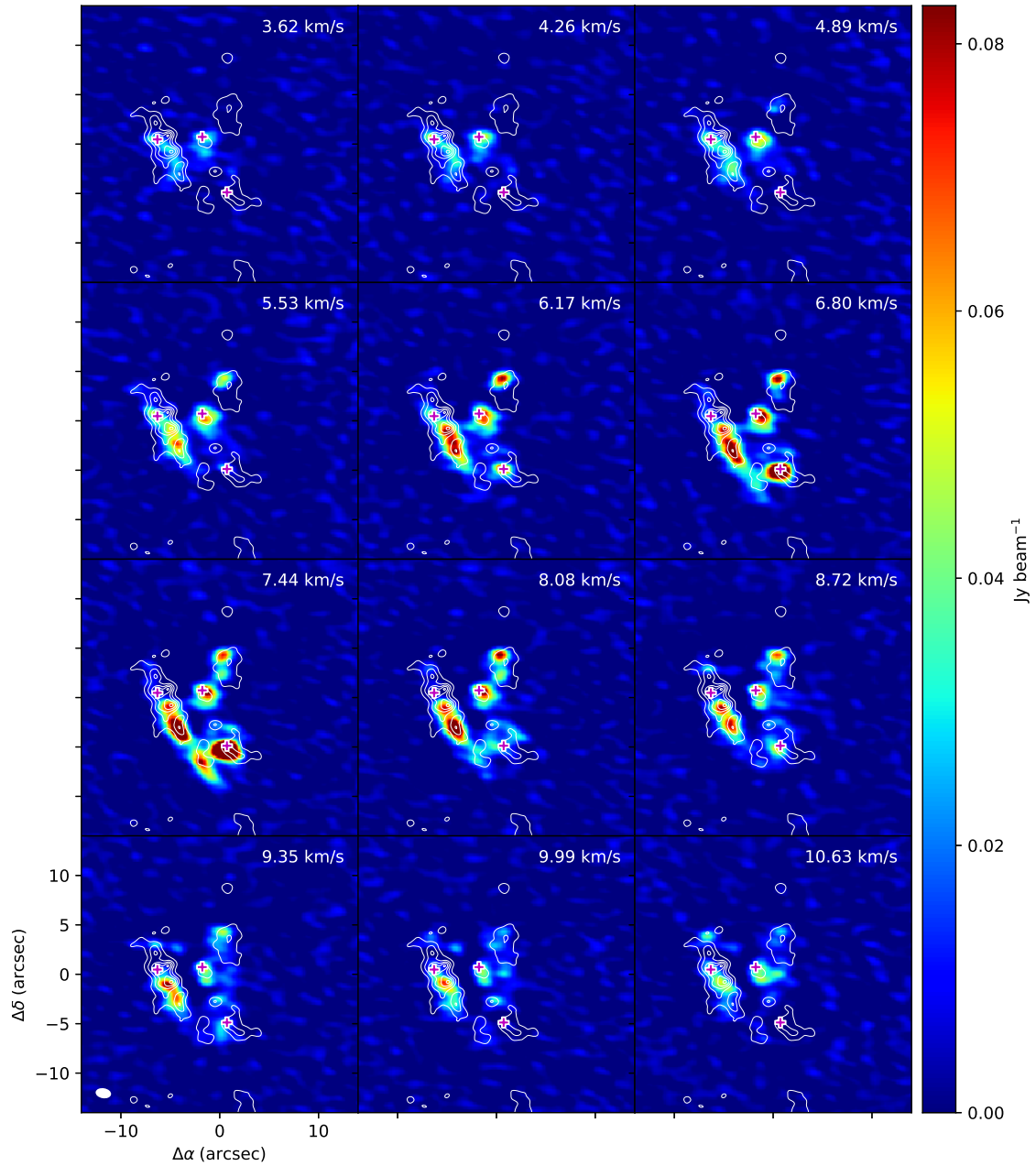


Figure 2.9: Channel map of expected unblended 229.908 GHz line.

2.3.2 Spectrum

The spectrum were extracted from the region of 1''.0 in diameter around Hot core ($\text{RA}_{J2000} : 05^{\text{h}}35^{\text{m}}14^{\text{s}}.580$, $\text{Dec}_{J2000} : -05^{\circ}22'31''.029$), and the Gaussian fitting was performed to obtain the line width and V_{lsr} of the emission line.

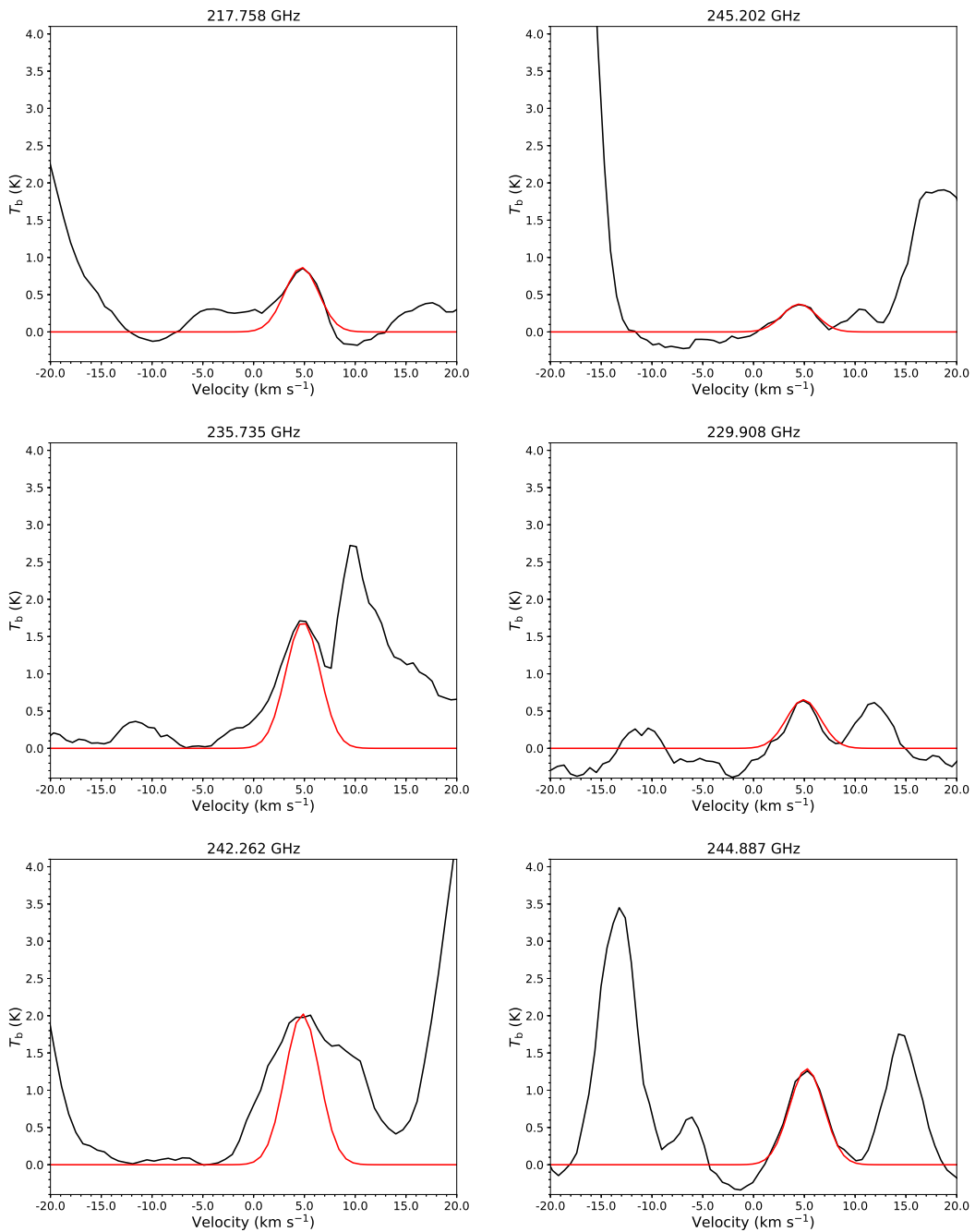


Figure 2.10: Spectrum of the CH_3NH_2 lines at each frequency observed in Hot core center (black) and the result of the Gaussian fitting (red).

2.4 Disuccion

2.4.1 Column density and Rotation temperature

In this subsection we will describe the methodologies in deriving fractional abundances of COMs. The column density of CH_3NH_2 (N_{MA}) was established by using the rotational temperature diagram method, which assumes local thermodynamic equilibrium (LTE) and optically thin emission. The following equation was employed for the analysis (Turner, 1991):

$$\log \frac{3 k_{\text{B}} T_{\text{B}} \Delta V_{1/2}}{8 \pi^3 \nu S \mu_0^2} = \log \frac{N_{\text{MA}}}{U_{\text{rot}}} - \frac{E_{\text{u}} \log e}{k_{\text{B}} T_{\text{rot}}} \quad (2.1)$$

In the expression, ν is the rest frequency of the transition, μ_0 is the permanent dipole moment, U_{rot} is the rotational partition function, S is the line strength, E_{u} is the upper state energy, and T_{B} and $\Delta V_{1/2}$ are the brightness temperature and line widths (FWHM, in km s^{-1}), respectively. We assumed $\Delta V_{1/2} = 4.0 \text{ km s}^{-1}$, which derived by the Gaussian fitting for 217.758 GHz line.

The brightness temperature can be converted from intensity I_{ν} when the Rayleigh-Jeans law is applicable.

$$T_{\text{B}} = \frac{c^2}{2 k_{\text{B}} \nu^2} I_{\nu} \quad (2.2)$$

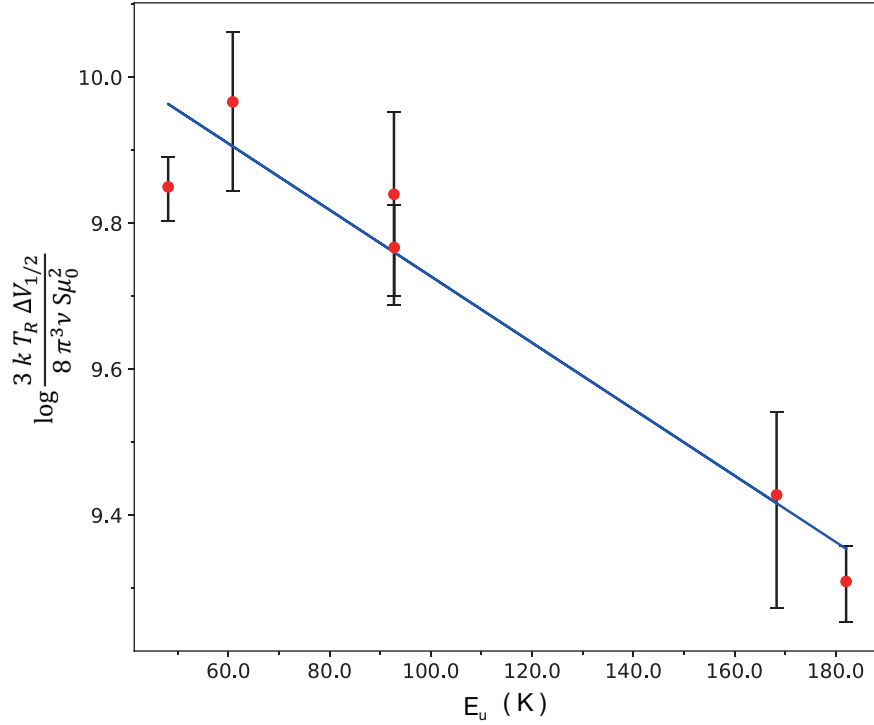


Figure 2.11: Rotation diagram of CH_3NH_2 in Hot core. The error bars represents $\pm 3\sigma$ for each data.

The resulting plots are given in Figure 2.11. The analysis yields a rotational temperature of $T_{\text{rot}} = 95.4^{+15.5}_{-11.7}$ K, with a column density of $N_{\text{MA}} = (5.5^{+1.6}_{-1.1}) \times 10^{14}$ cm $^{-2}$.

2.4.2 Undetectable lines

Comparison of catalogs did not suggest contamination, but some emission lines could not be detected as CH_3NH_2 .

Table 2.3: transitions of CH_3NH_2

Frequency [GHz]	$S\mu^2$ [D 2]	E_u [K]	Transition (J, K_a, Γ)	peak T_B [K]	V_{LSR} [km s $^{-1}$]	Noise [K]	Comments
215.670	53.92	111.48	9, 2, $E_{1-1} \rightarrow 9, 1, E_{1+1}$	3.74(0.07)	5.37(0.07)	0.043	
221.755	35.06	133.11	10, 2, $A_2 \rightarrow 10, 1, A_1$	0.33(0.03)	5.35(0.19)	0.133	SV data

As shown in Figure 2.12, the CH_3NH_2 data including 2 transitions in Table 2.3 produced point-to-point scatter perhaps because of the lower signal-to-noise ratio for the

weaker transitions in SV data and possible low-level contamination.

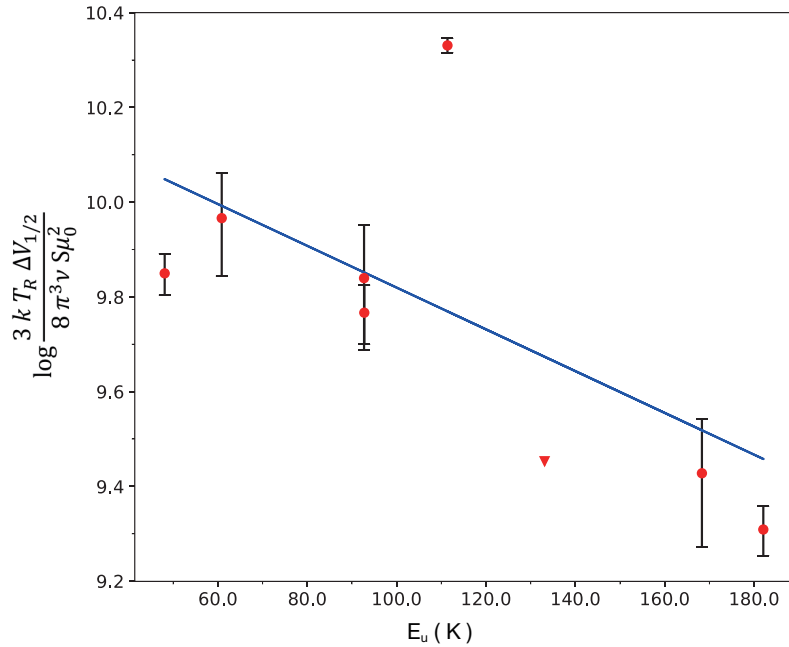
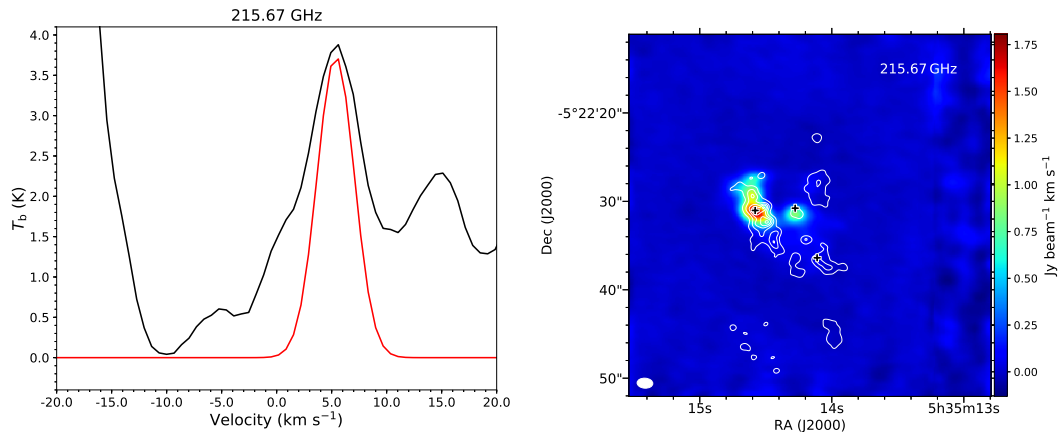


Figure 2.12: Rotation diagram of CH_3NH_2 in Hot core with more 2 lines. The error bars represents $\pm 3 \sigma$ for each data. Upper limit is indicated with triangle. ※ 6 点のみ用いた一次関数と、ノイズレベルの上限も含めた図に差し替え

215.670 GHz line



(c) 左の図の説明

(d) 右の図の説明

Figure 2.13: 215GHz.

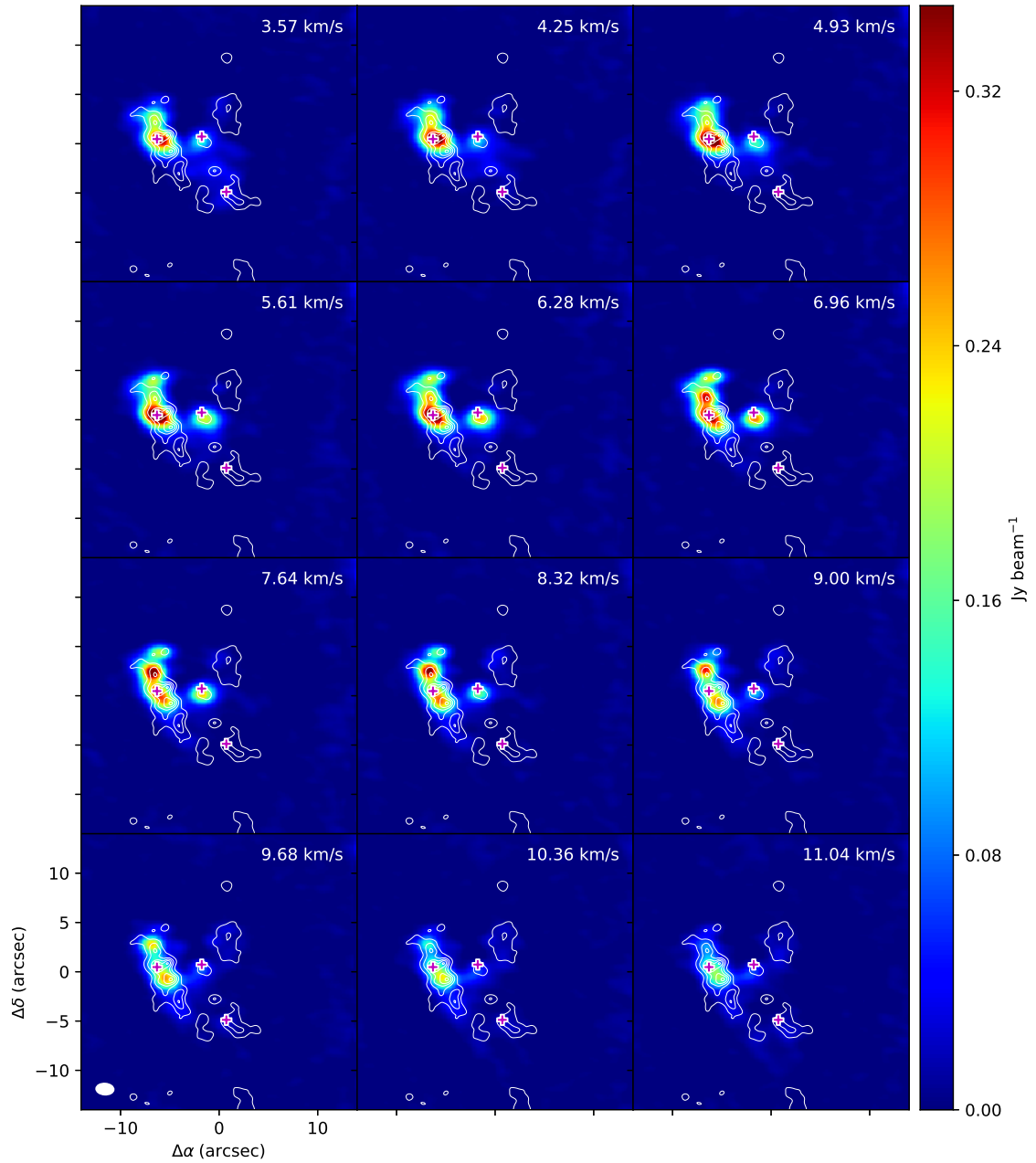
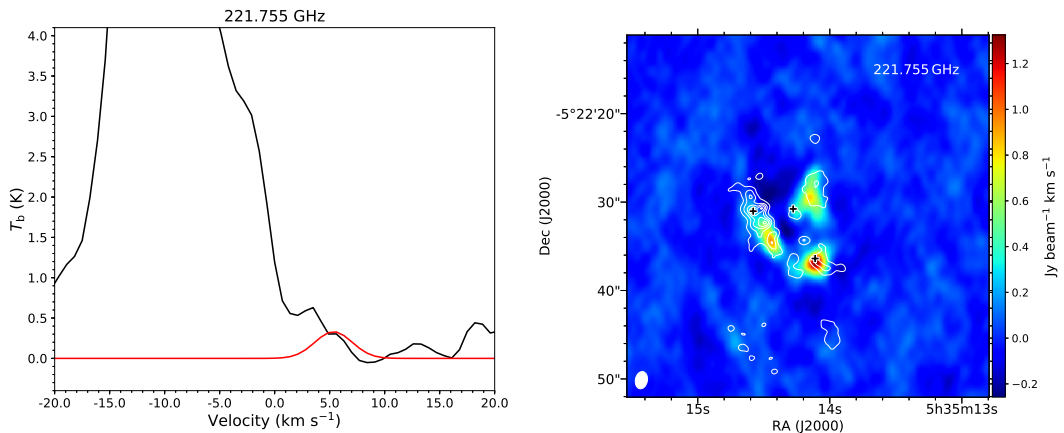


Figure 2.14: Channel map of expected unblended 215.670 GHz line.

221.755 GHz line



(c) 左の図の説明

(d) 右の図の説明

Figure 2.15: 221.755 GHz.

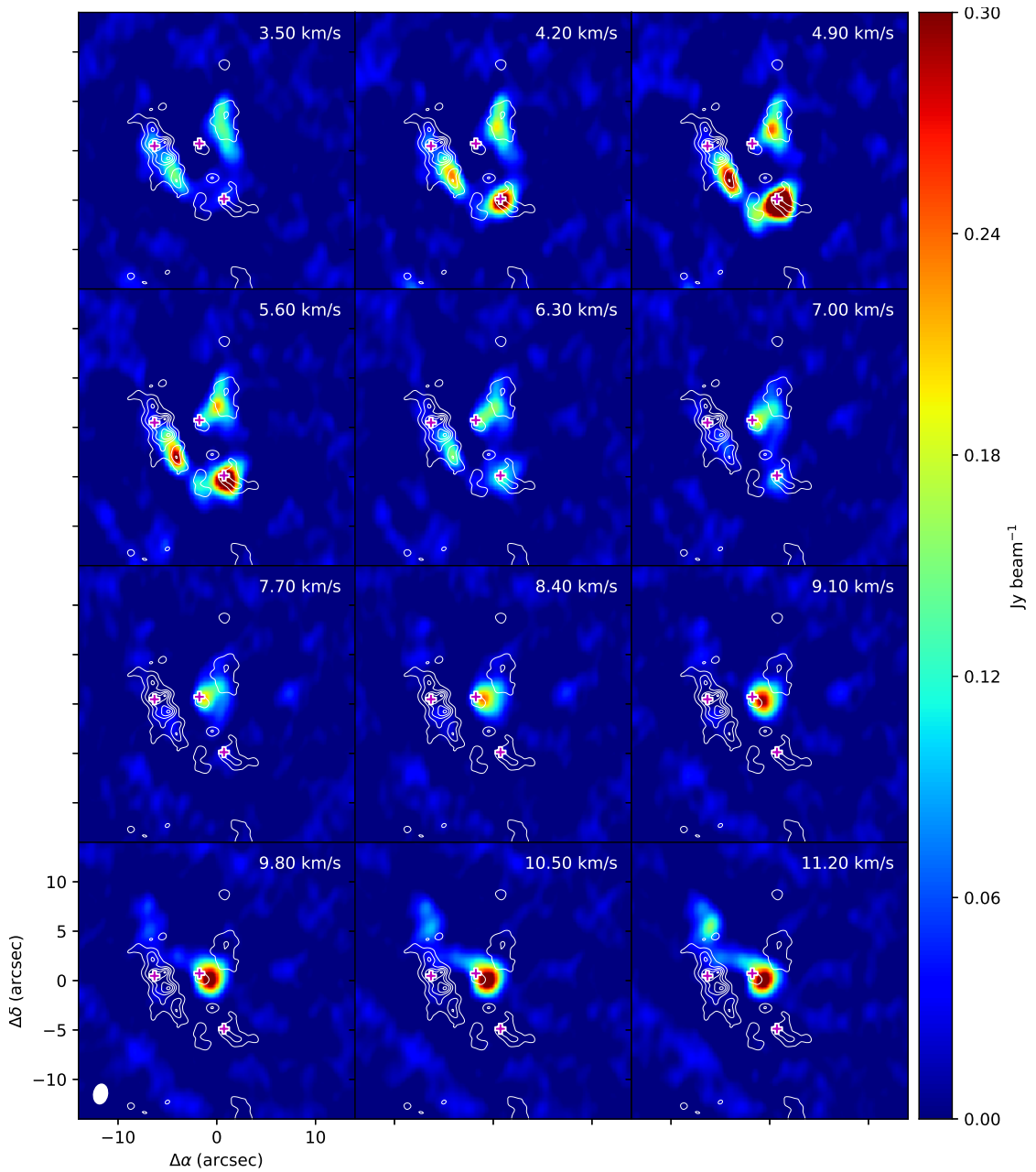


Figure 2.16: Channel map of expected unblended 221.755 GHz line.

Chapter 3

Methylamine survey in low mass star-forming regions

3.1 Review of low mass star-forming region

3.2 Analysis

3.3 IRAS 16293

3.3.1 Observation data

3.3.2 Results

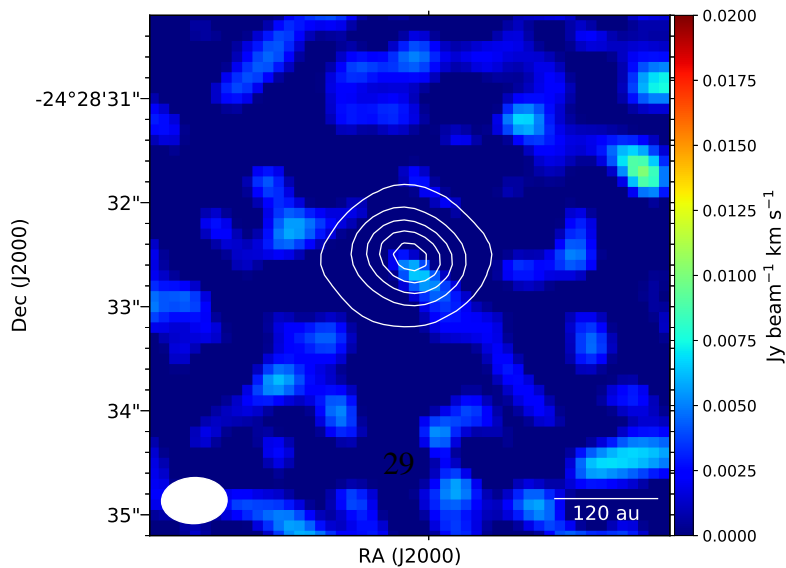


Figure 3.1: Integrated intensity map around 247.362 GHz. The white contours represent

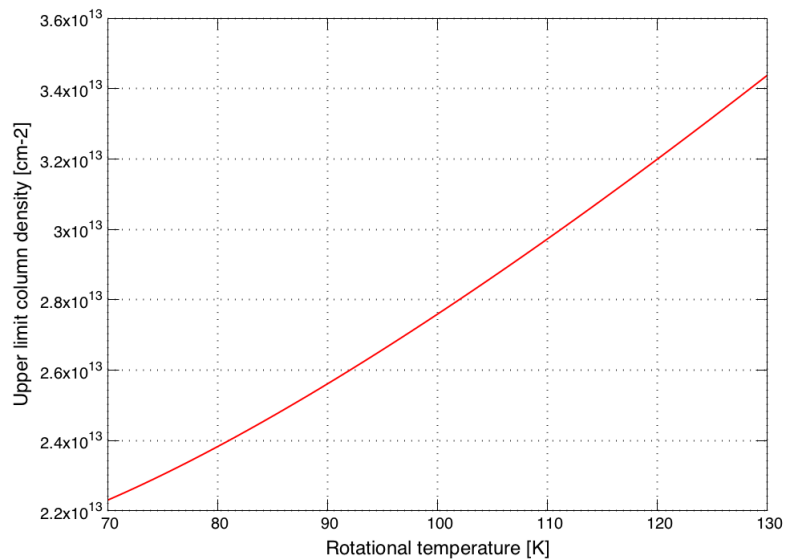


Figure 3.2: Upper limit column density for the strongest CH_3NH_2 transition ($7_2E_{1-1} \rightarrow 7_1E_{1-1}$) as function of T_{rot} . A 3σ value of $11.4 \text{ mJy beam}^{-1}$ is used.

3.4 L483

3.4.1 Observation data

3.4.2 Results

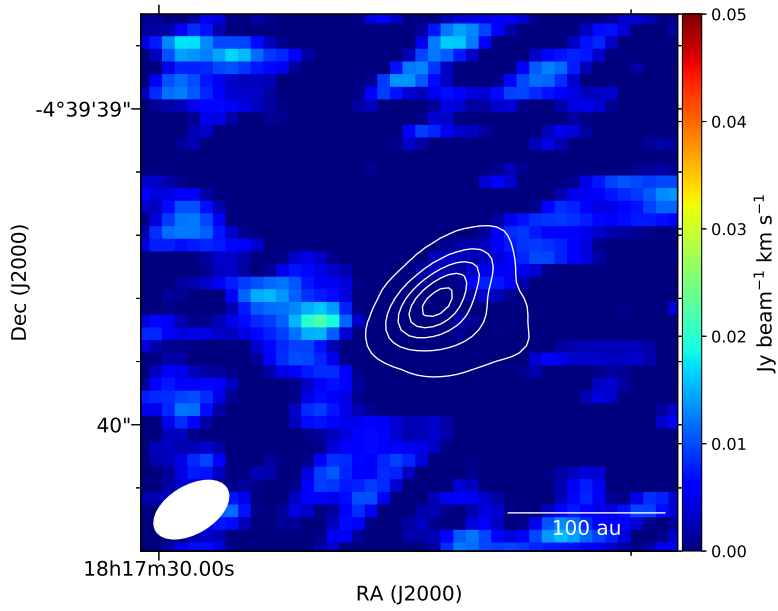


Figure 3.3: Integrated intensity map around 217.079 GHz. The white contours represent the 1.3 mm continuum map, where the contour levels are 10 %, 30 %, 50 %, 70 %, 90 % of the peak intensity.

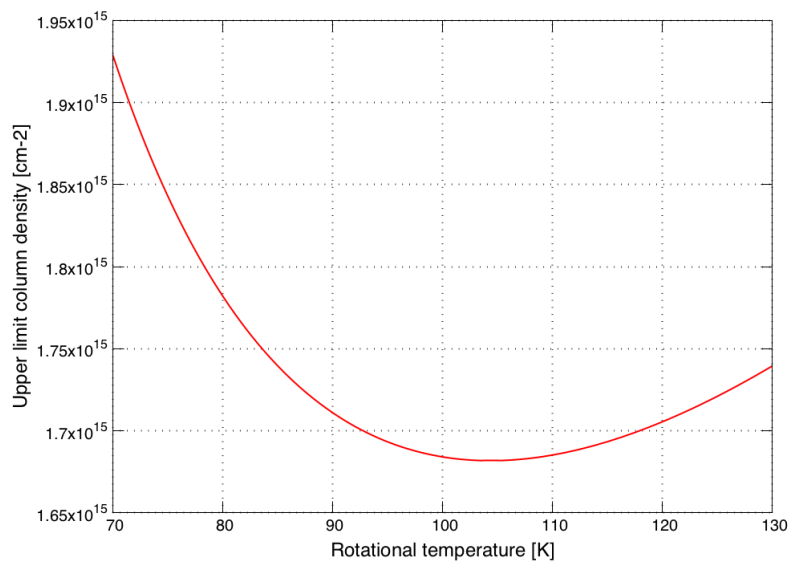


Figure 3.4: Upper limit column density for the strongest CH_3NH_2 transition ($11_2A_1 \rightarrow 11_2A_2$) as function of T_{rot} . A 3σ value of $22.5 \text{ mJy beam}^{-1}$ is used.

Chapter 4

Discussion

Chapter 5

Conclusions

Appendix A

Distribution of methylamine lines contaminated by other molecular line emission in Orion-KL

A.1 Integrated intensity maps

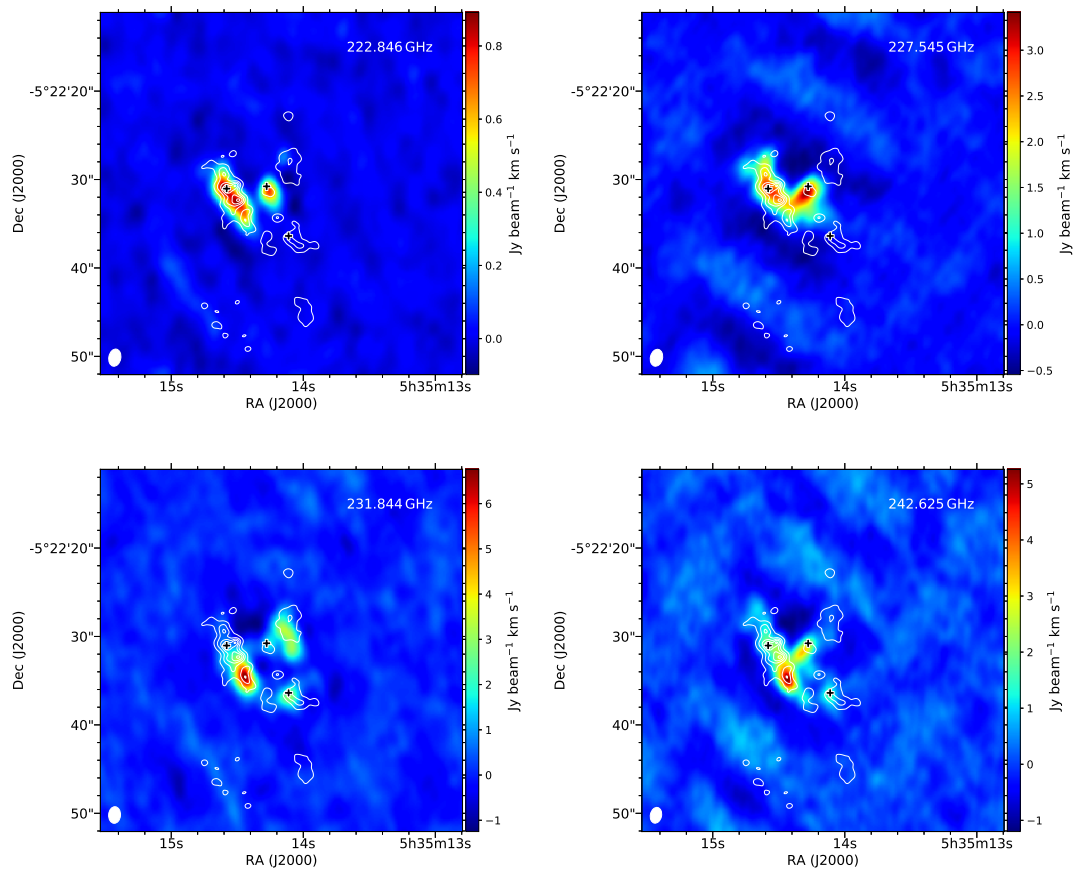


Figure A.1: Integrated intensity maps around methylamine line.

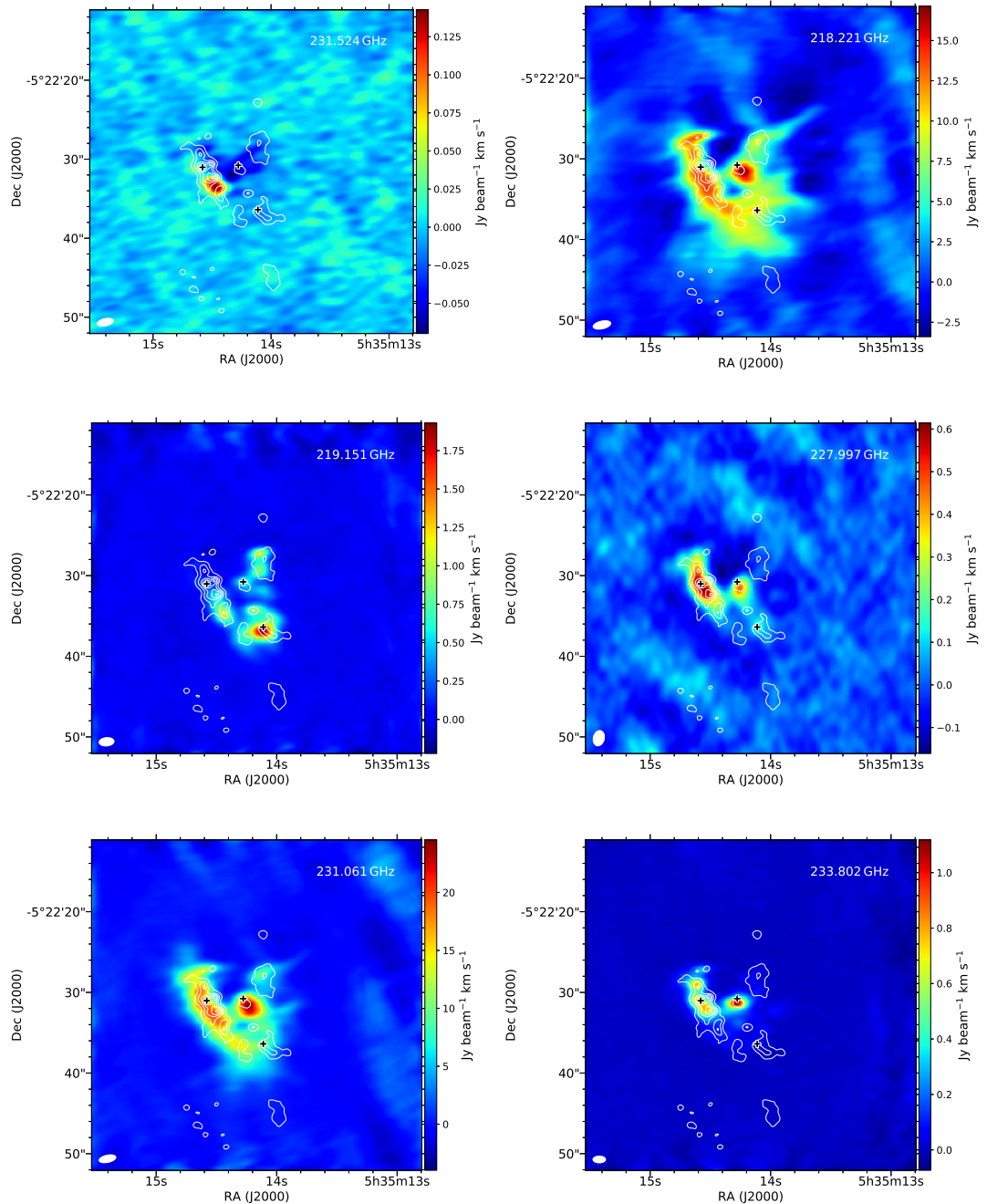


Figure A.2: (Continued)

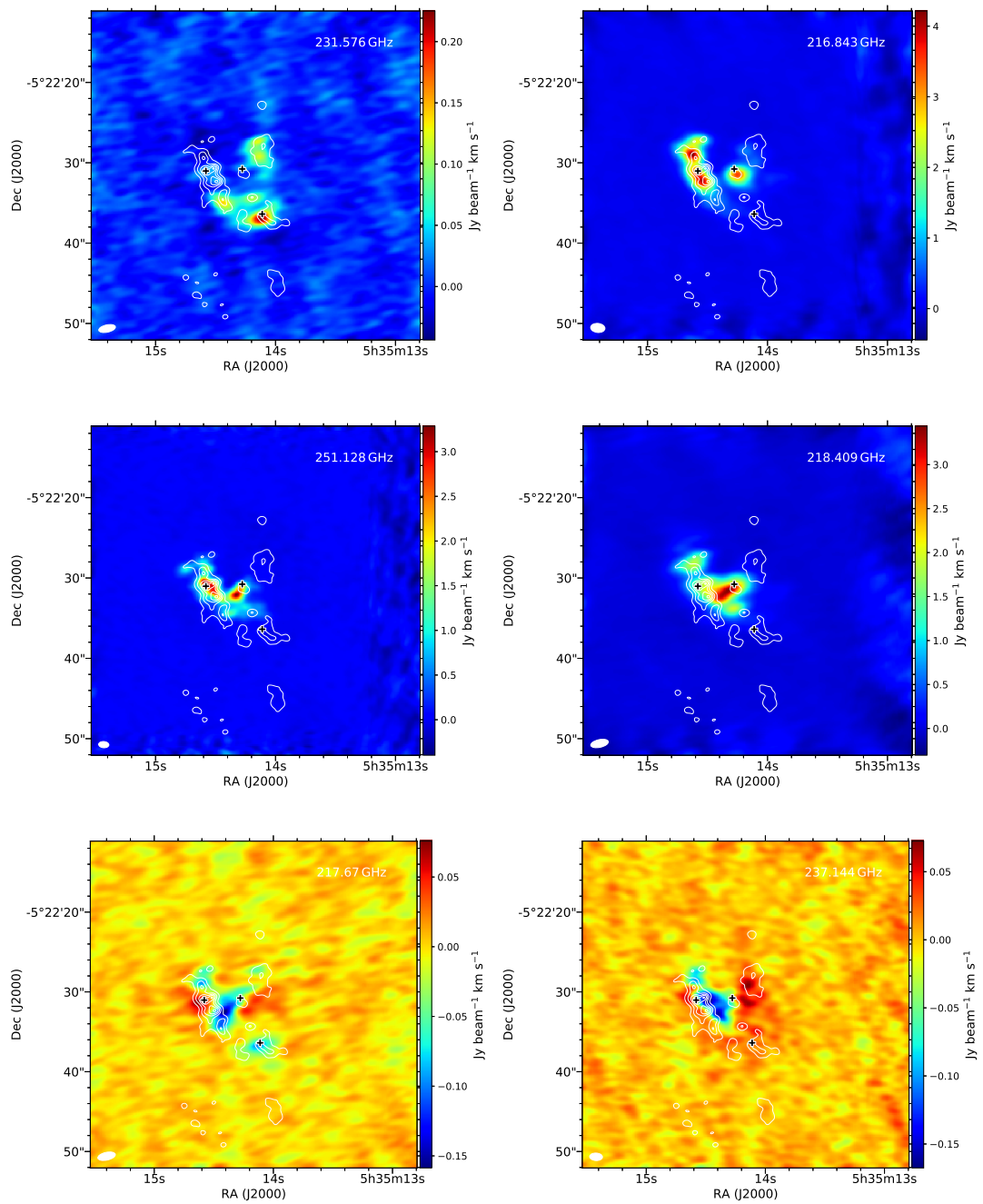


Figure A.3: (Continued)

A.2 Channel maps

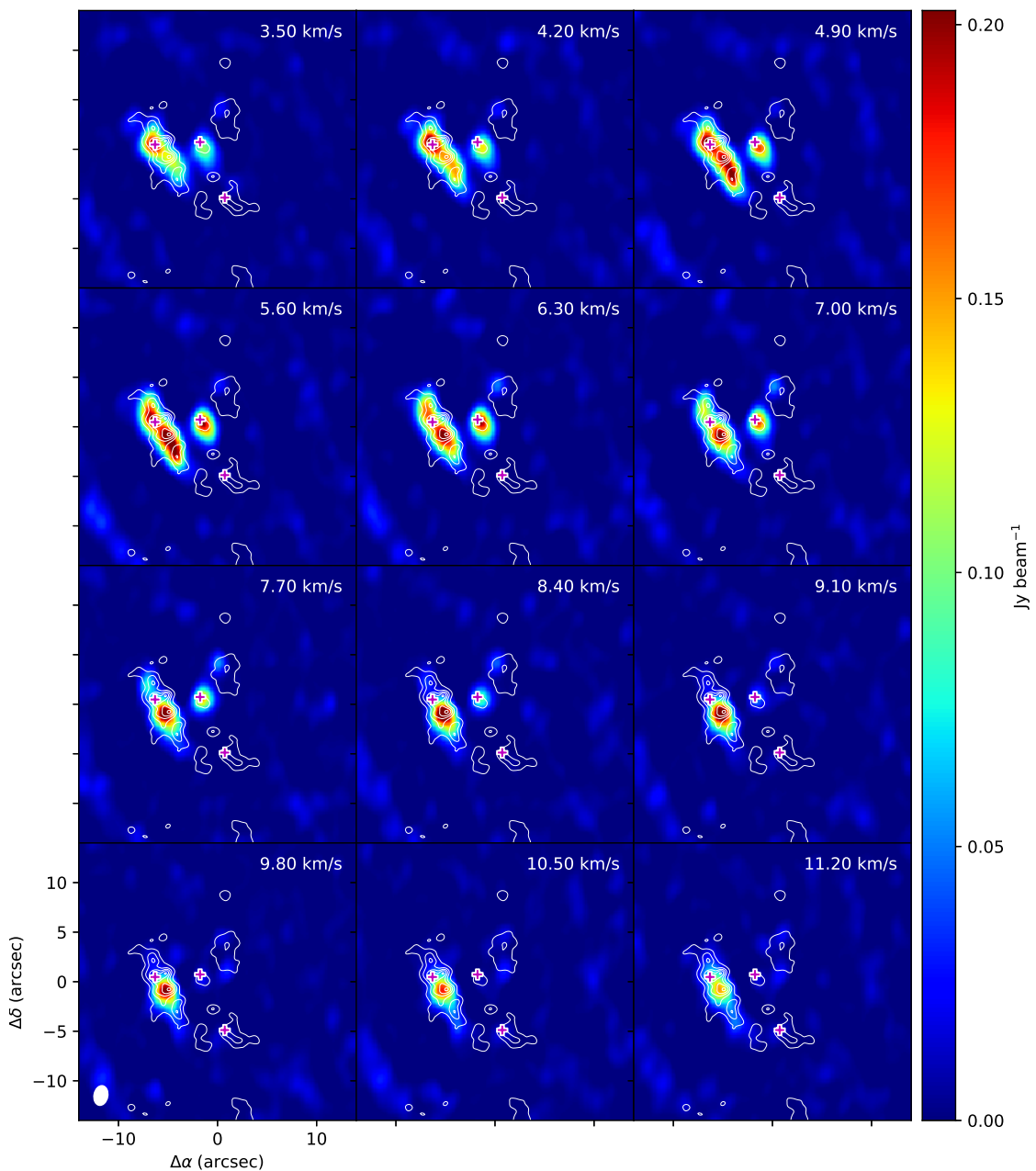


Figure A.4: 222.846GHz

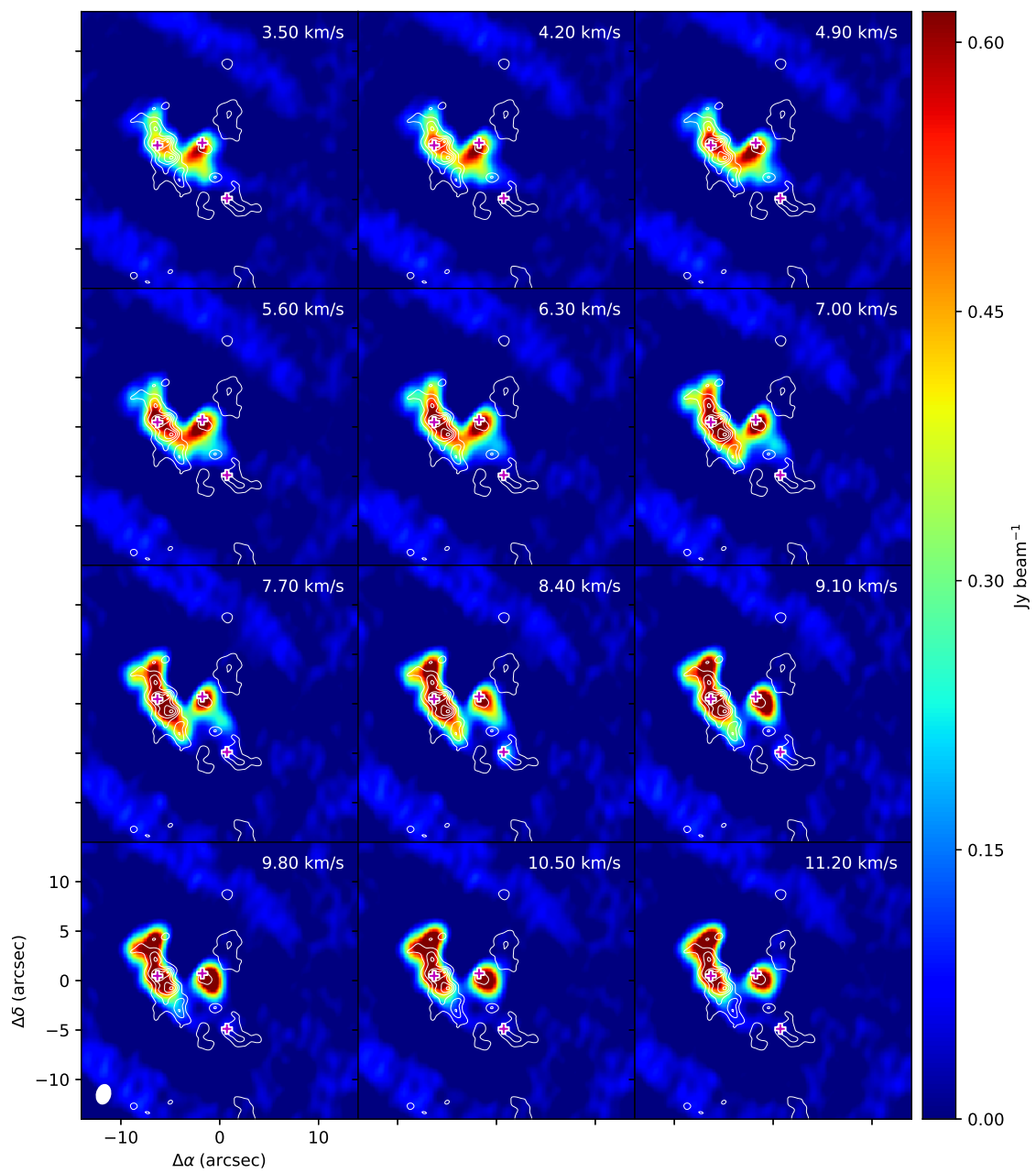


Figure A.5: 227.545GHz

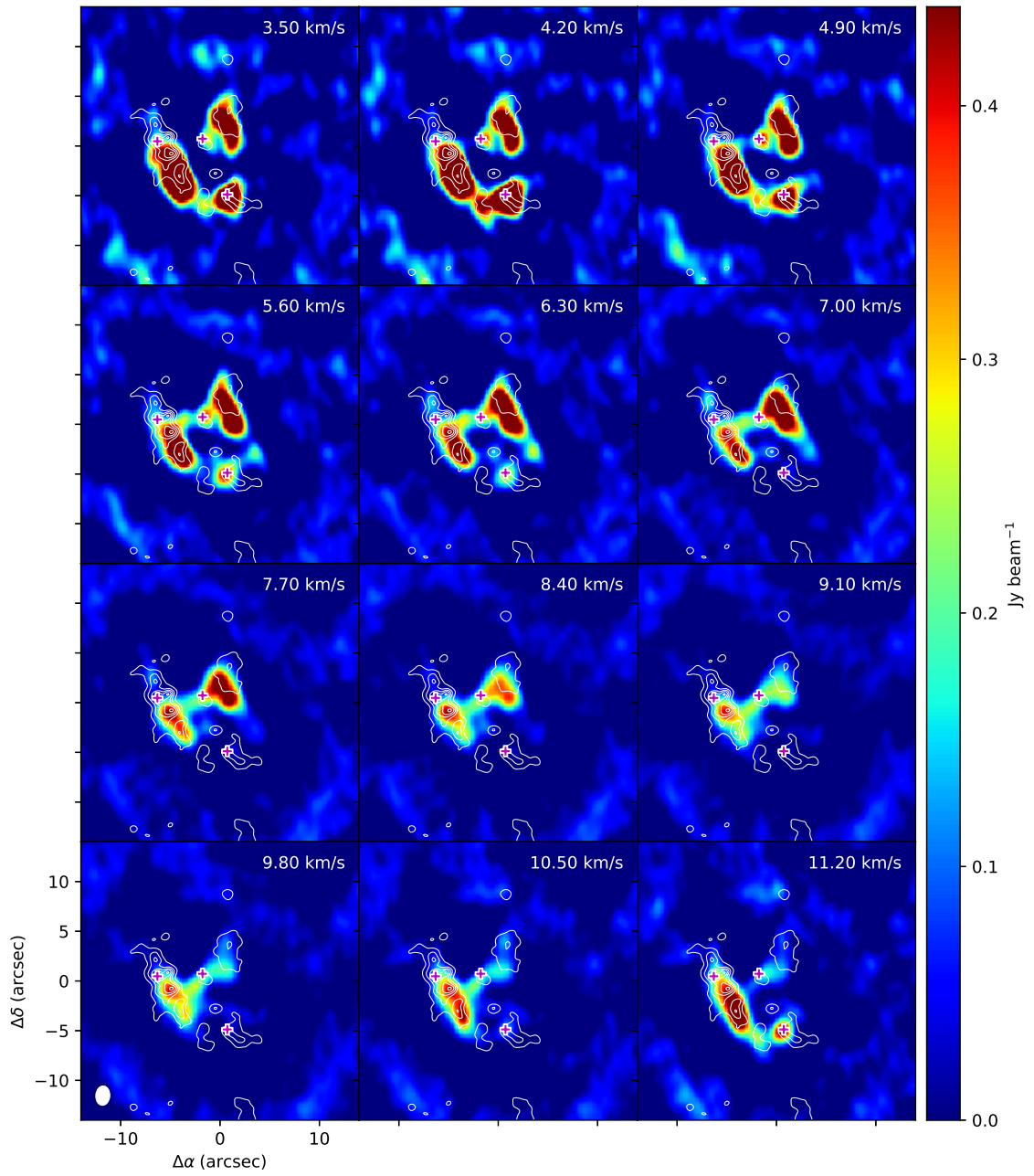


Figure A.6: 231.844GHz

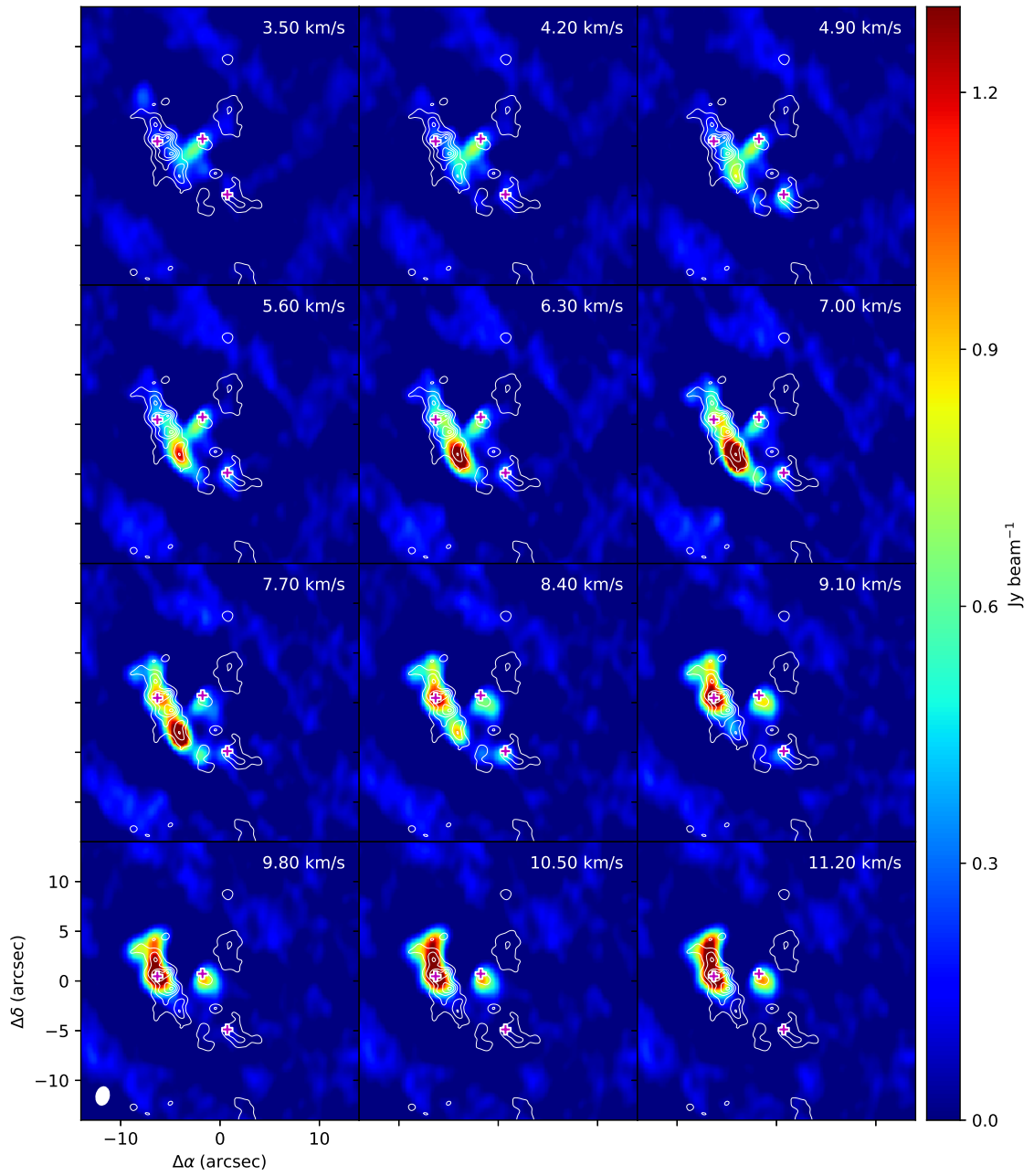


Figure A.7: 242.625GHz

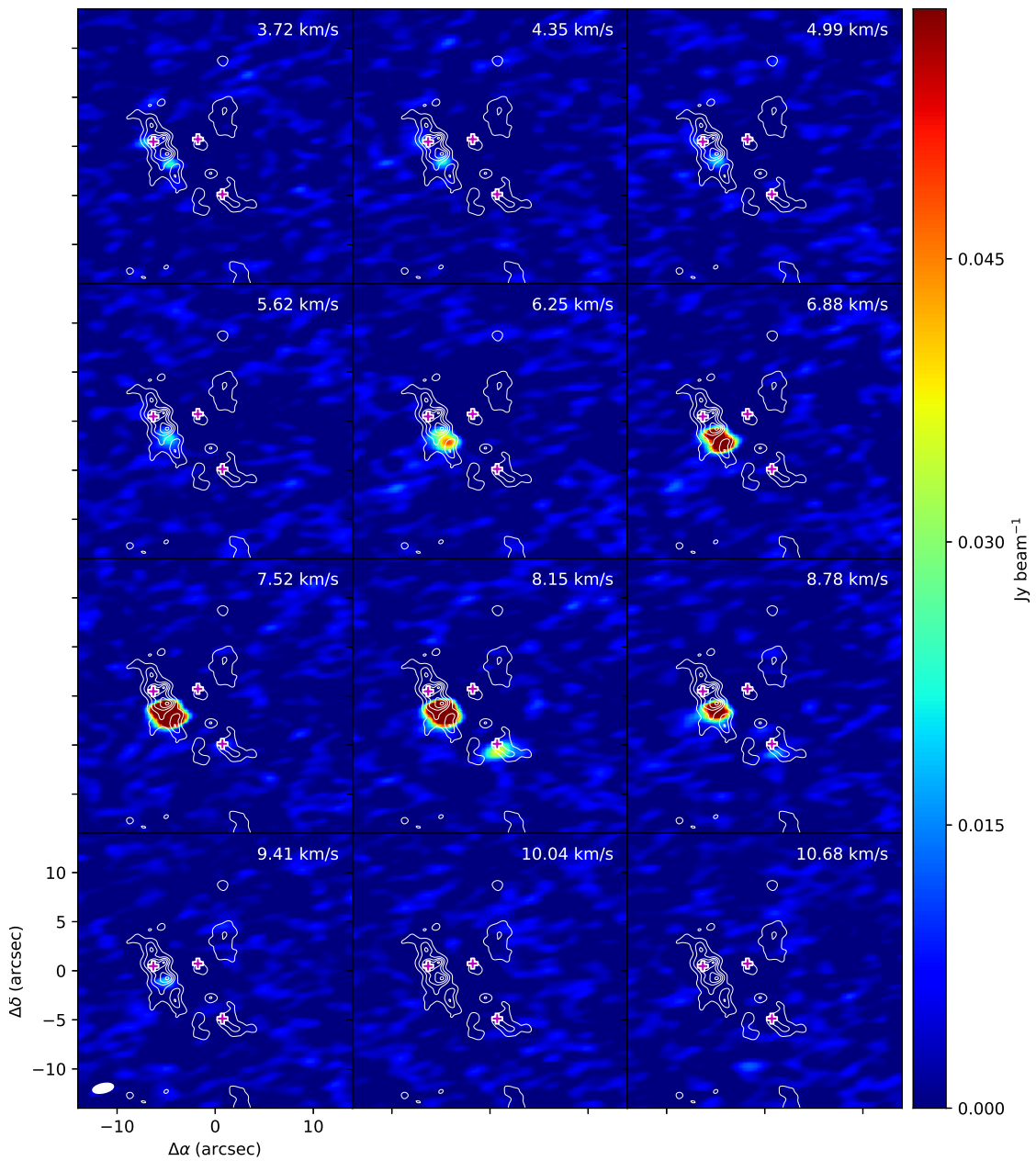


Figure A.8: 231.524GHz

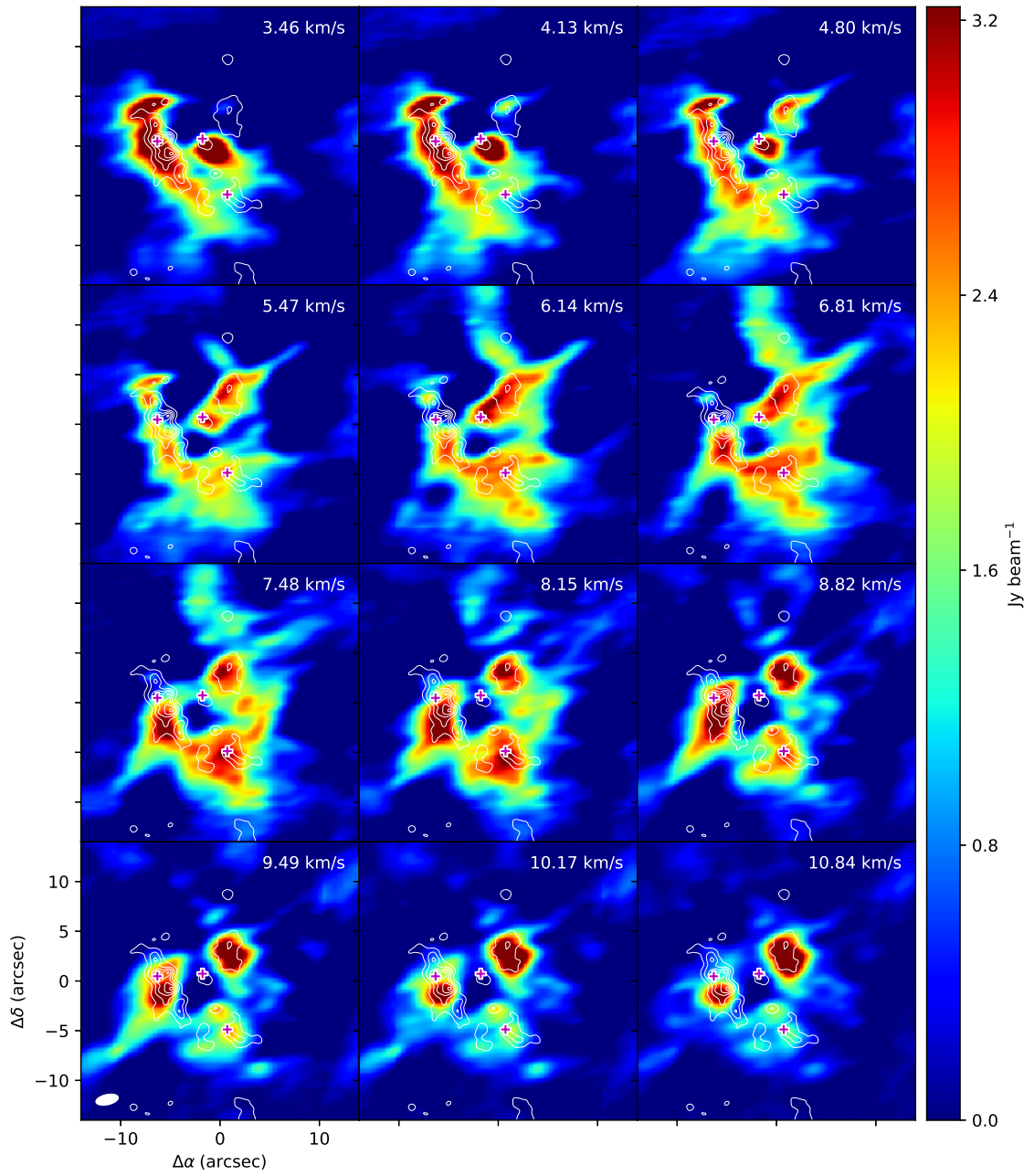


Figure A.9: 218.221GHz

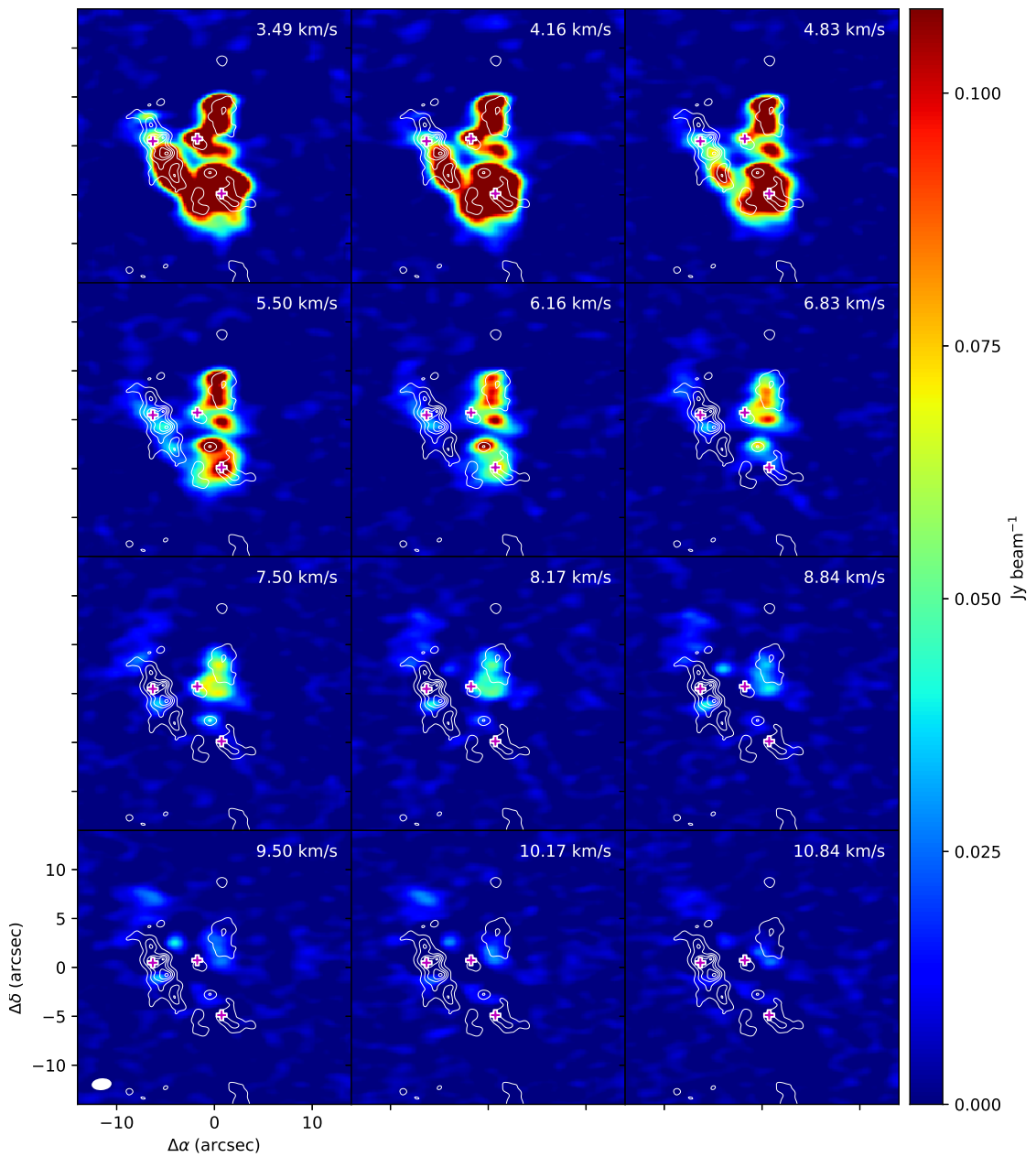


Figure A.10: 219.151GHz

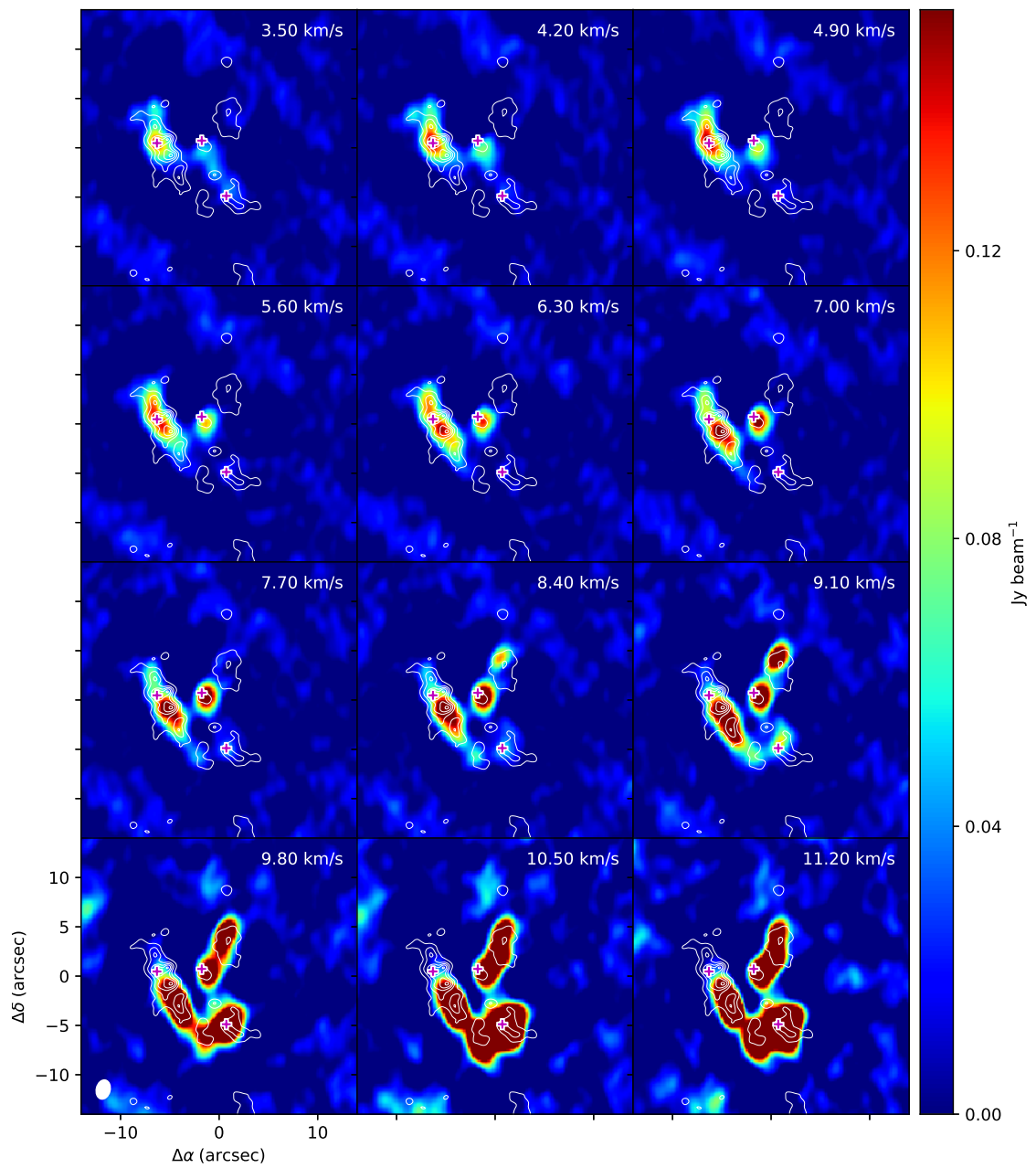


Figure A.11: 227.997GHz

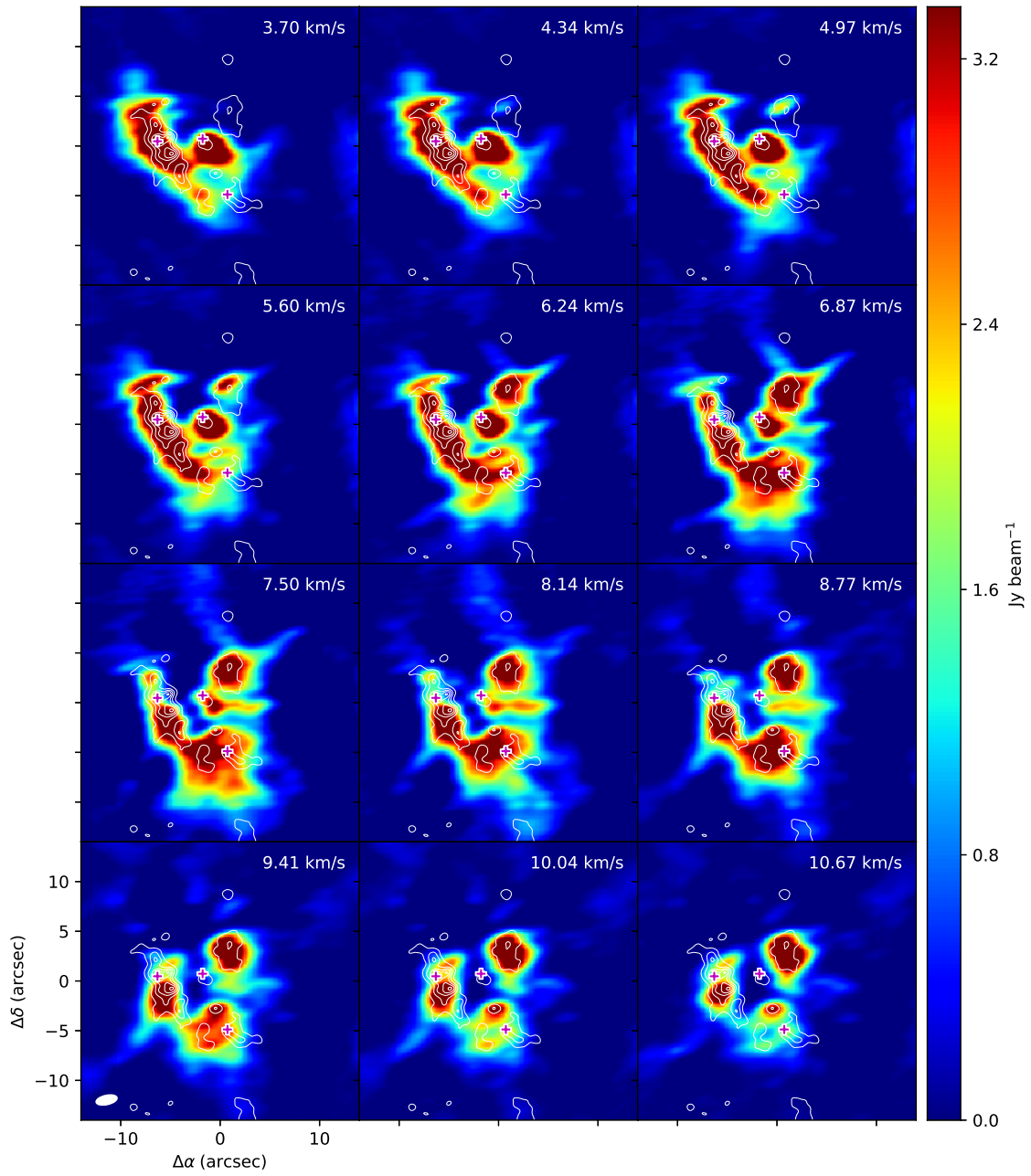


Figure A.12: 231.061GHz

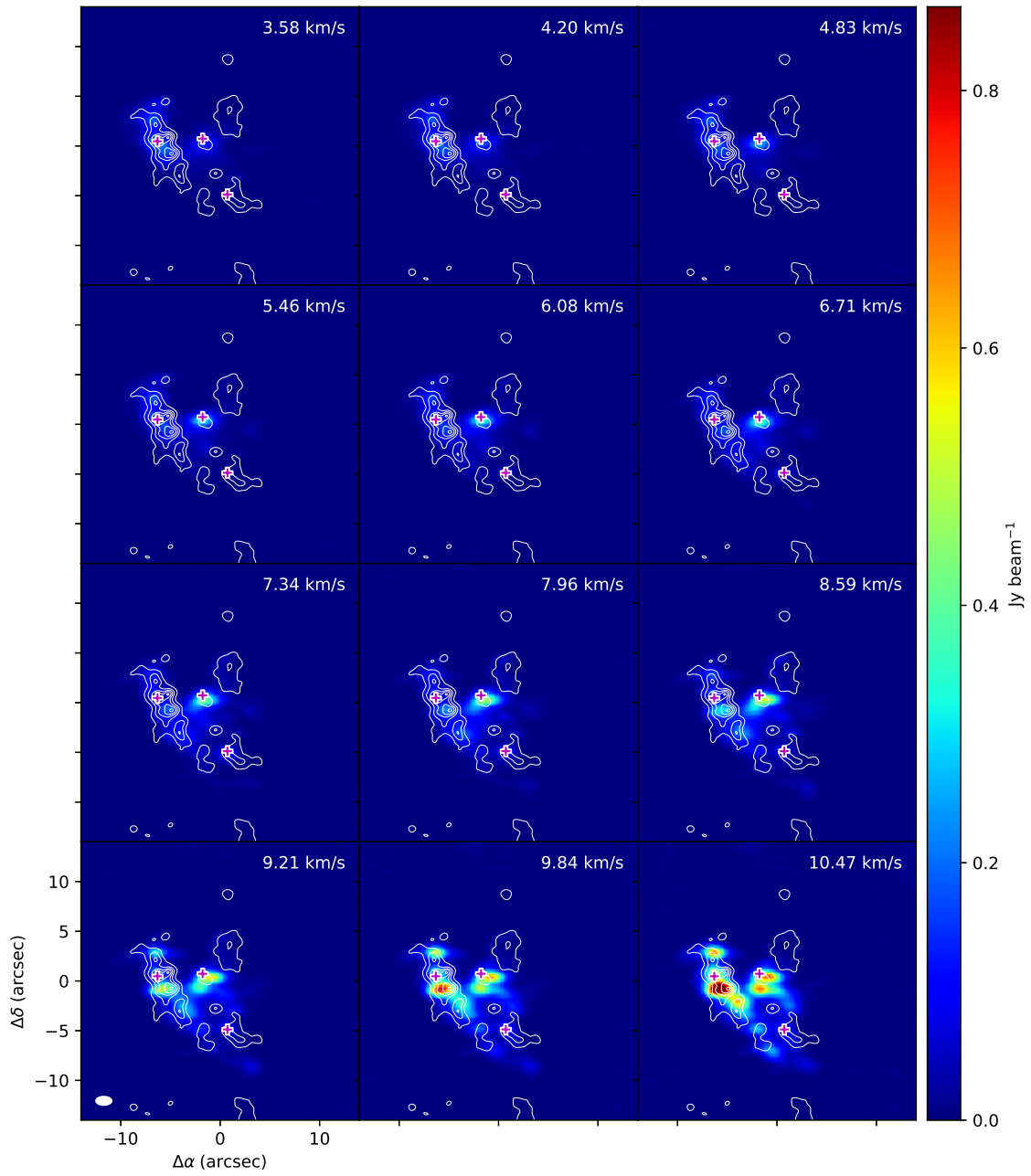


Figure A.13: 233.802GHz

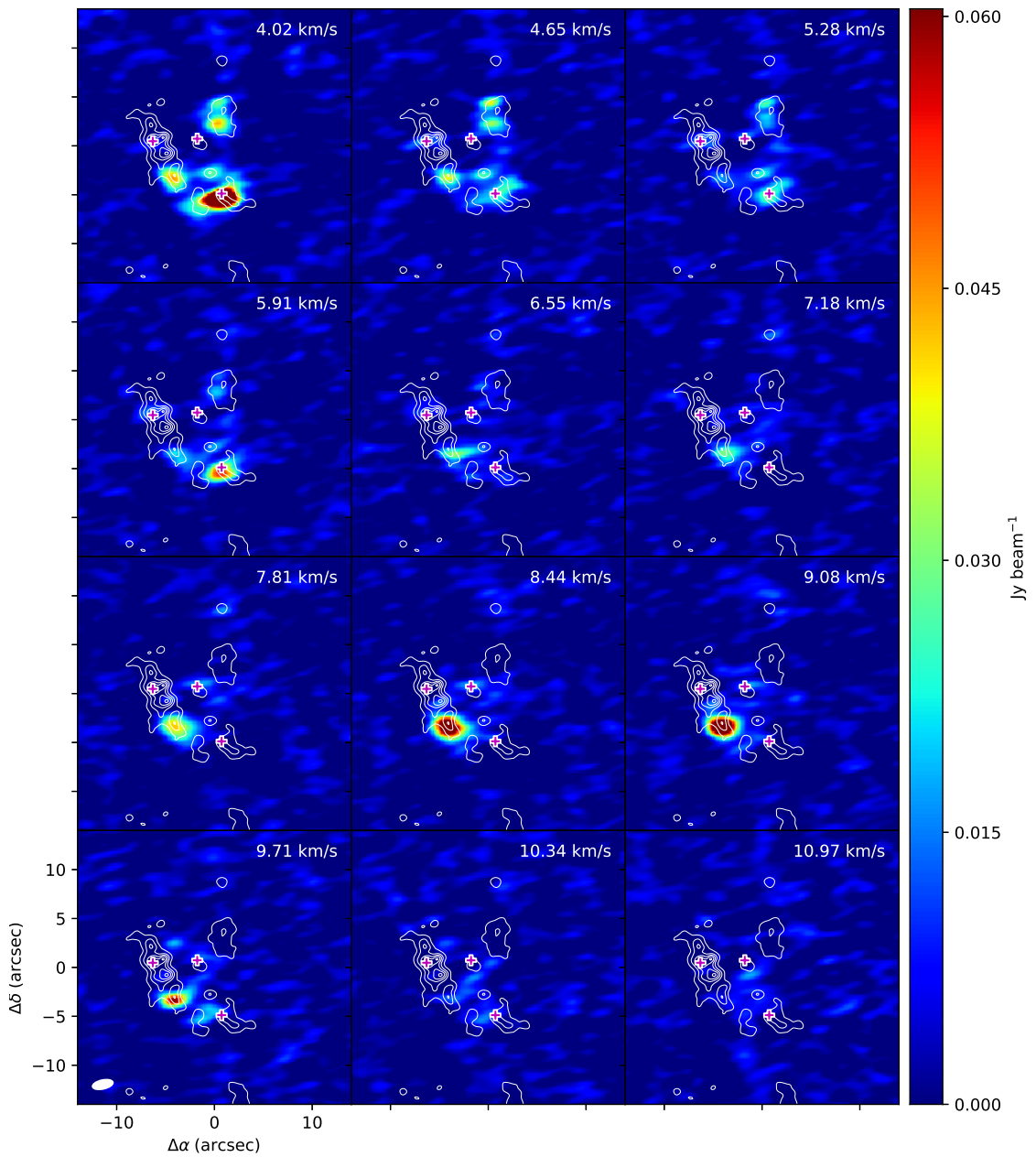


Figure A.14: 231.576GHz

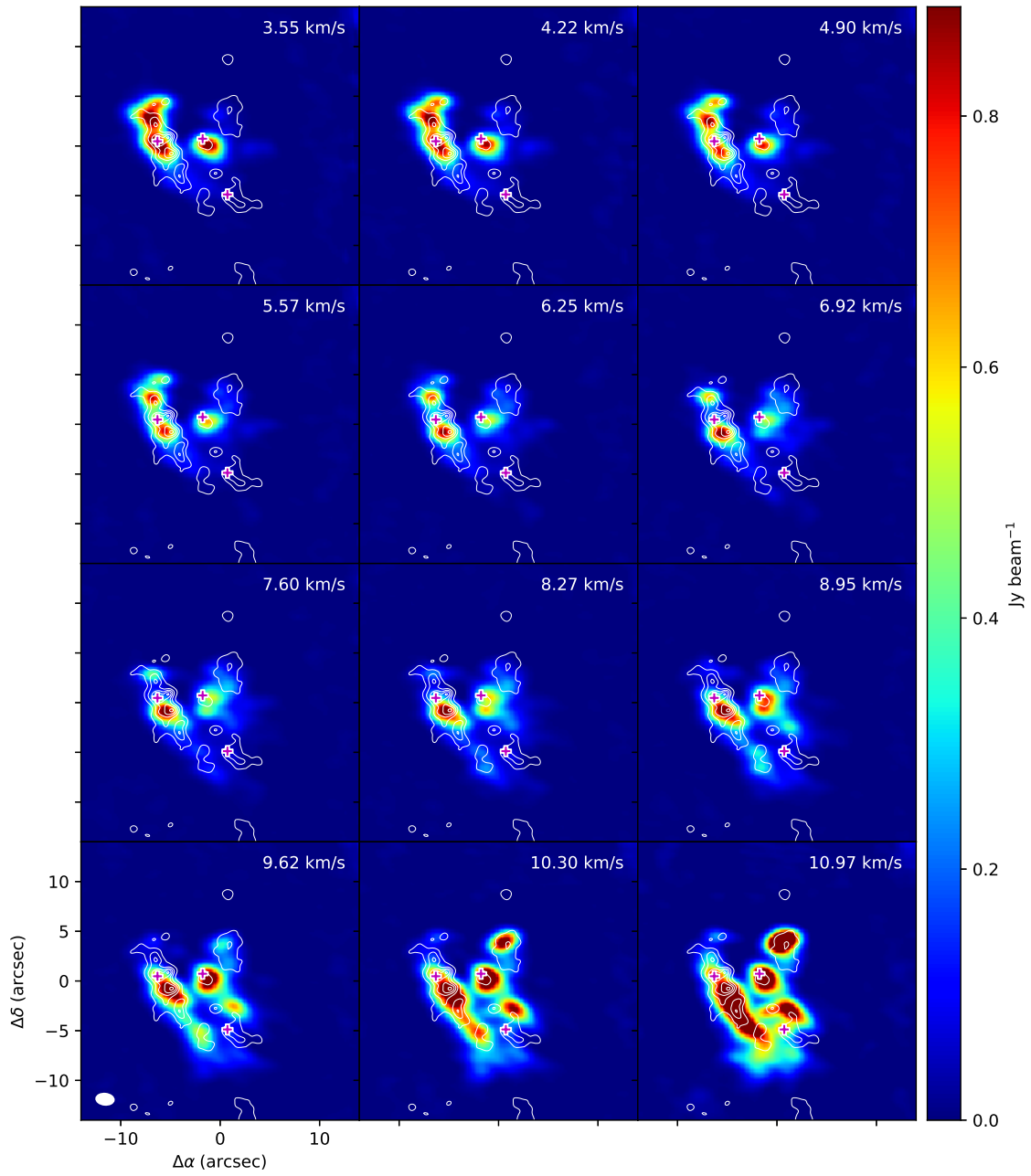


Figure A.15: 216.843GHz

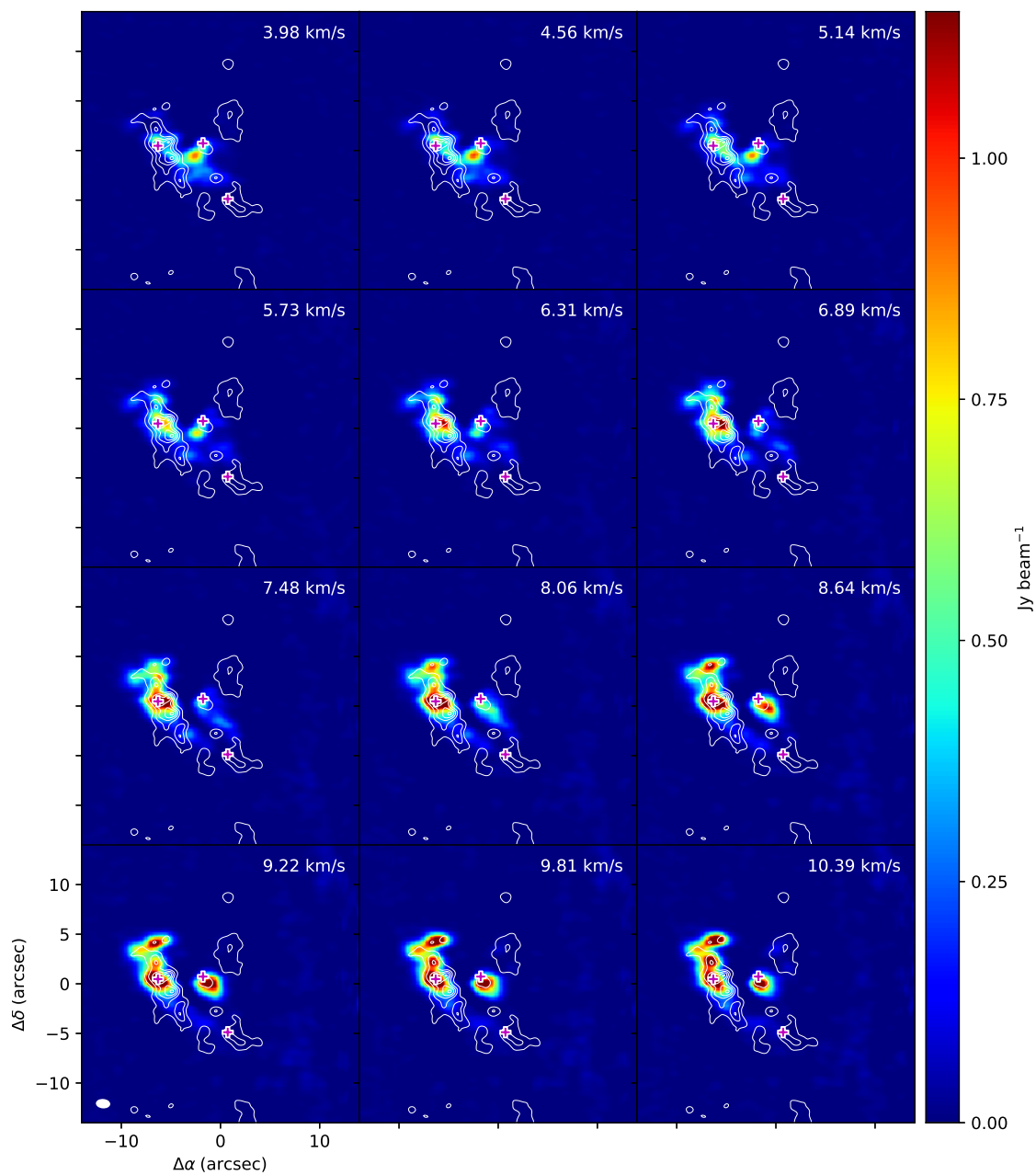


Figure A.16: 251.128GHz

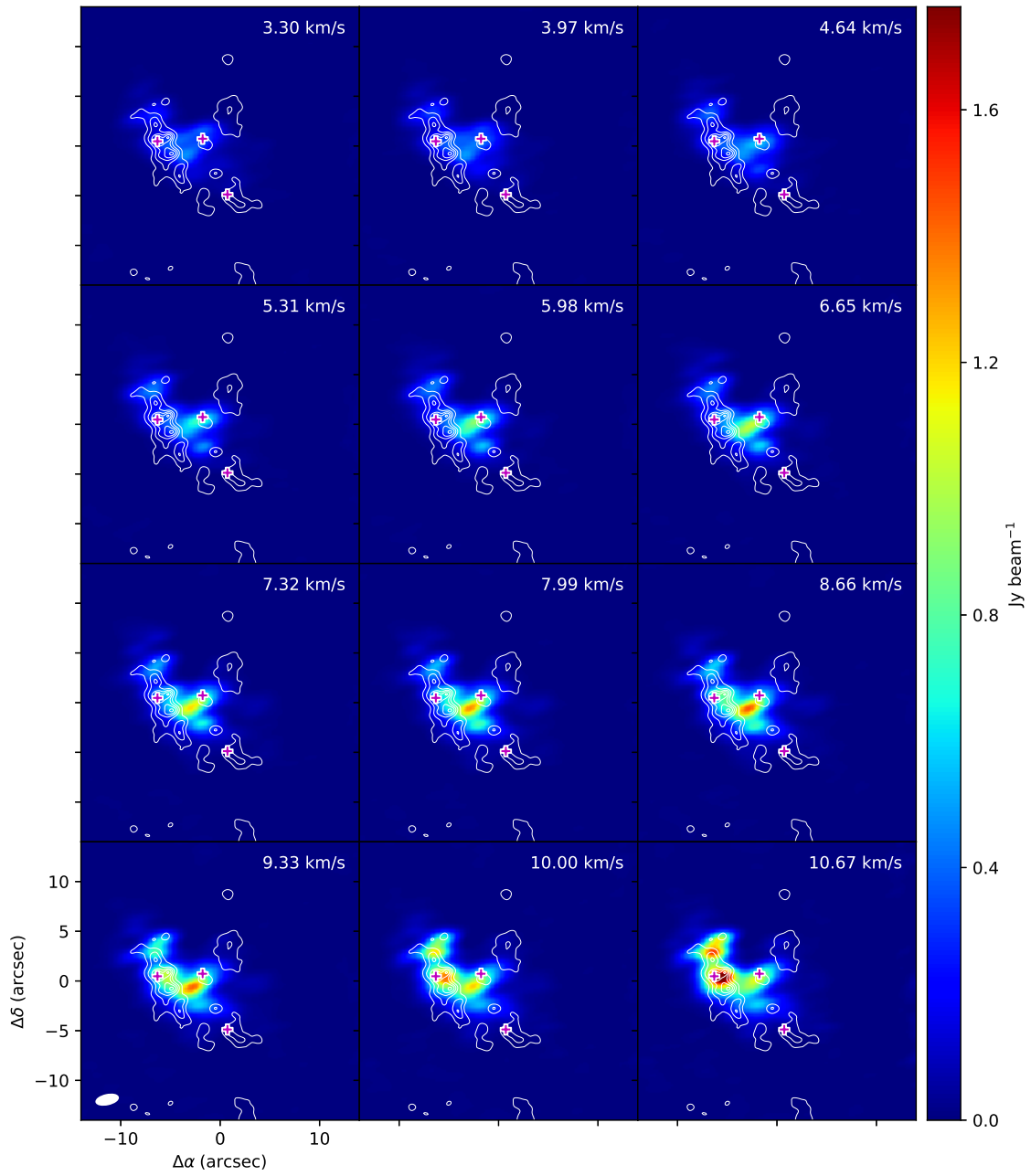


Figure A.17: 218.409GHz

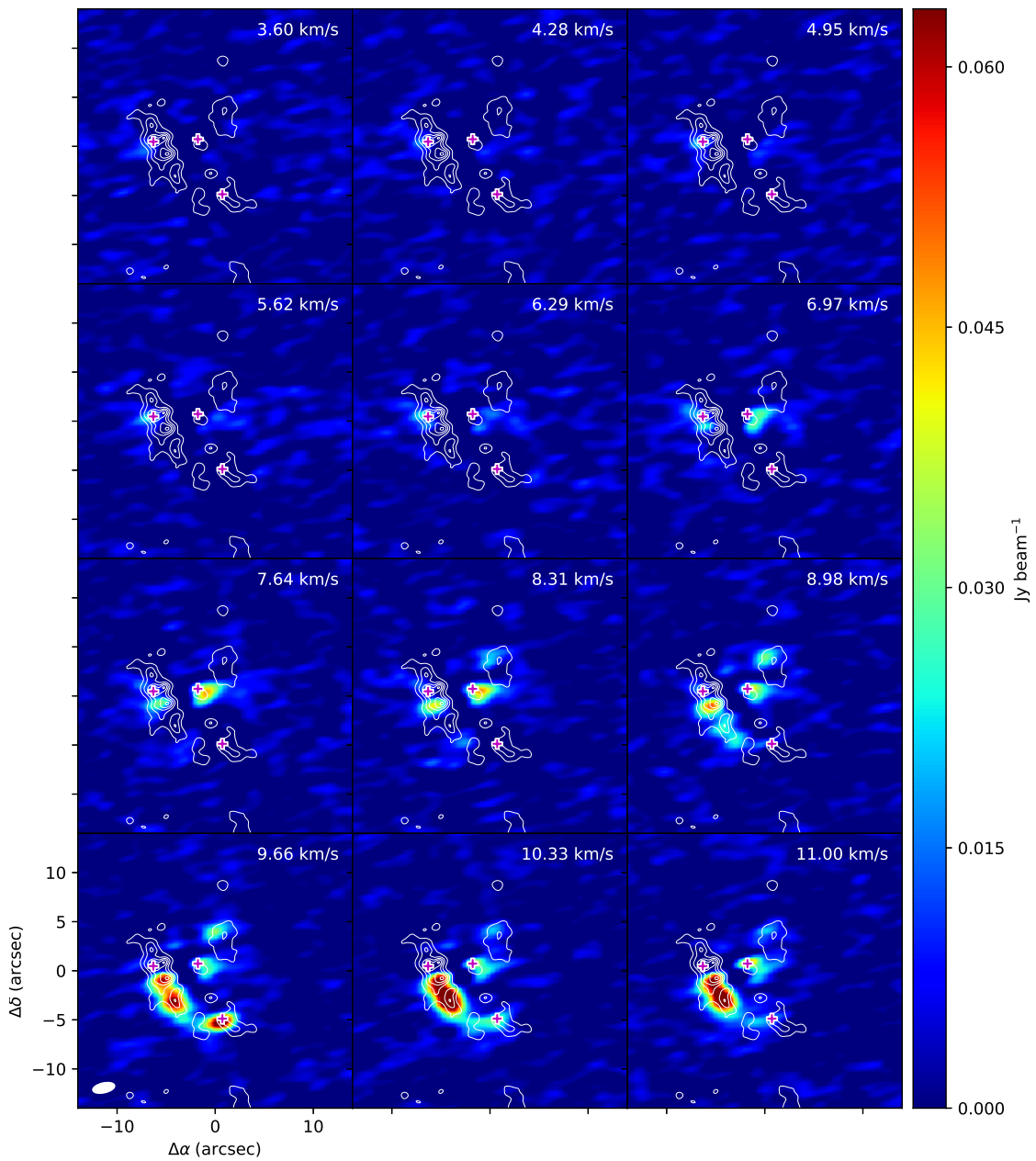


Figure A.18: 217.670GHz

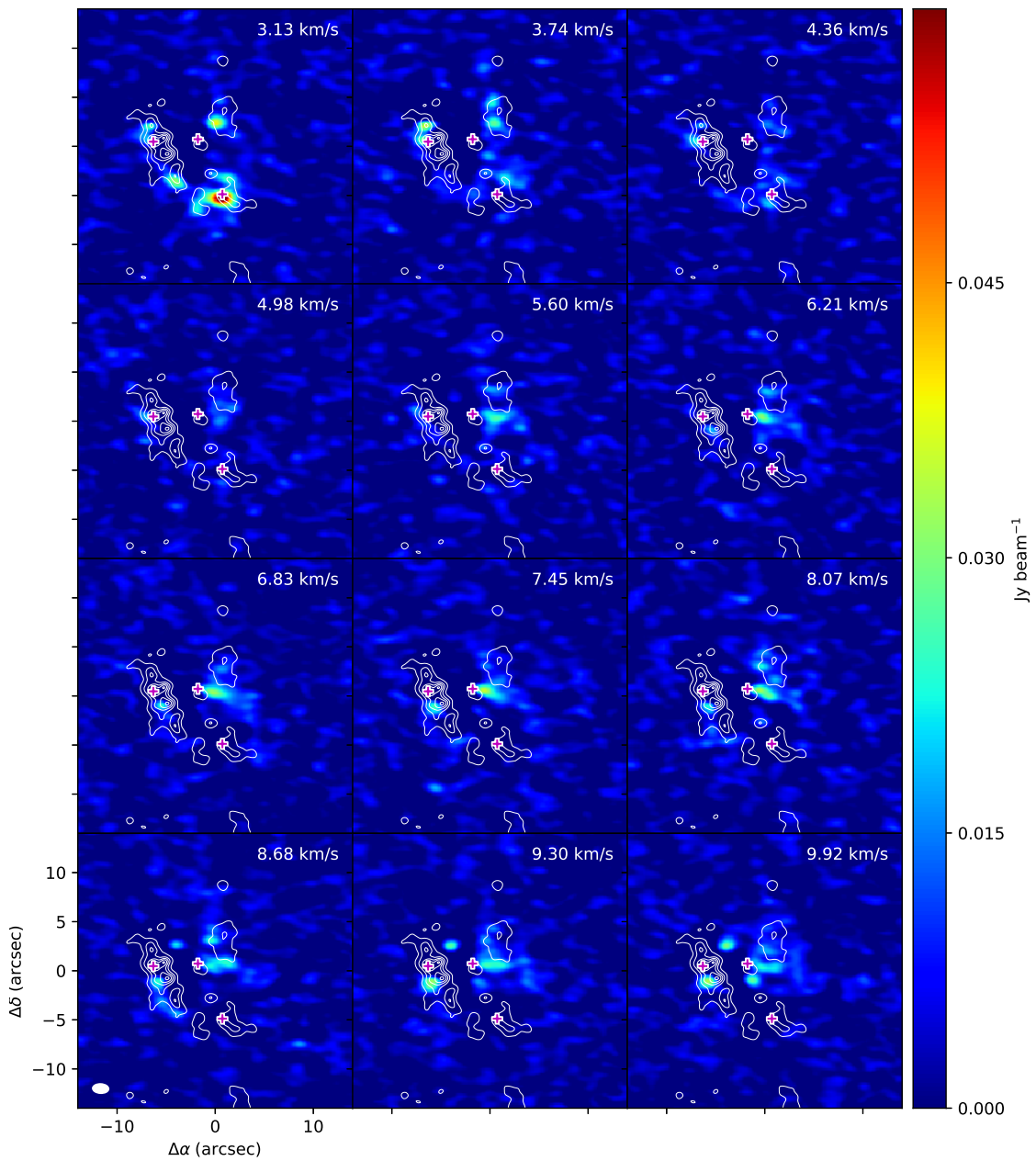


Figure A.19: 237.144GHz

Acknowledgments

References

- Altwegg, K., et al. 2016, *Science Advances*, 2, e1600285
- . 2017, *Monthly Notices of the Royal Astronomical Society*, 469, S130
- Bossa, J.-B., Duvernay, F., Theulé, P., Borget, F., D'Hendecourt, L., & Chiavassa, T. 2009, *Astronomy & Astrophysics*, 506, 601
- Ehrenfreund, P., Bernstein, M. P., Dworkin, J. P., Sandford, S. A., & Allamandola, L. J. 2001, *The Astrophysical Journal Letters*, 550, L95
- Feng, S., Beuther, H., Henning, T., Semenov, D., Palau, A., & Mills, E. A. C. 2015, *Astronomy & Astrophysics*, 581, A71
- Fourikis, N., Takagi, K., & Morimoto, M. 1974, *The Astrophysical Journal Letters*, 191, L139
- Glavin, D. P., Dworkin, J. P., & Sandford, S. A. 2008, *Meteoritics and Planetary Science*, 43, 399
- Gong, Y., et al. 2015, *Astronomy & Astrophysics*, 581, A48
- Hirota, T., Kim, M. K., Kurono, Y., & Honma, M. 2015, *The Astrophysical Journal*, 801, 82
- Holtom, P. D., Bennett, C. J., Osamura, Y., Mason, N. J., & Kaiser, R. I. 2005, *The Astrophysical Journal*, 626, 940

- Kaifu, N., Morimoto, M., Nagane, K., Akabane, K., Iguchi, T., & Takagi, K. 1974, The Astrophysical Journal Letters, 191, L135
- Kounkel, M., et al. 2017, The Astrophysical Journal, 834, 142
- Lee, C.-W., Kim, J.-K., Moon, E.-S., Minh, Y. C., & Kang, H. 2009, The Astrophysical Journal, 697, 428
- McMullin, J. P., Waters, B., Schiebel, D., Young, W., & Golap, K. 2007, in Astronomical Society of the Pacific Conference Series, Vol. 376, Astronomical Data Analysis Software and Systems XVI, ed. R. A. Shaw, F. Hill, & D. J. Bell, 127
- Motiyenko, R. A., Ilyushin, V. V., Drouin, B. J., Yu, S., & Margulès, L. 2014, Astronomy & Astrophysics, 563, A137
- Pagani, L., Favre, C., Goldsmith, P. F., Bergin, E. A., Snell, R., & Melnick, G. 2017, Astronomy & Astrophysics, 604, A32
- Sanchez-Monge, A., Schilke, P., Ginsburg, A., Cesaroni, R., & Schmiedeke, A. 2017, STATCONT: Statistical continuum level determination method for line-rich sources, Astrophysics Source Code Library
- Turner, B. E. 1991, The Astrophysical Journal Supplement, 76, 617